Remarks on A_2 Toda Theory[1]

S. A. Apikyan[1, *] and C. J. Efthimiou[2, 1, **]

[1] *Department of Theoretical Physics, Yerevan State University, 375049 Yerevan, Armenia*
*e-mail: apikyan@lx2.yerphi.am
[2] *Department of Physics, University of Central Florida, FL 32816 Orlando, USA*
**e-mail: costas@physics.ucf.edu

We study the Toda field theory with finite Lie algebras using an extension of the Goulian–Li technique. In this way, we show that, after integrating over the zero mode in the correlation functions of the exponential fields, the resulting correlation function resembles that of a free theory. Furthermore, it is shown that for some ratios of the charges of the exponential fields the four-point correlation functions which contain a degenerate field satisfy the Riemann ordinary differential equation. Using this fact and the crossing symmetry, we derive a set of functional equations for the structure constants of the A_2 Toda field theory. © 2001 MAIK "Nauka/Interperiodica".

PACS numbers: 11.10.Kk

1. The Toda field theory (TFT) provides an extremely useful description of a large class of two-dimensional integrable quantum field theories. For this reason, these models have attracted considerable interest in recent years and many outstanding results in various directions have been established.

TFTs are divided into three broad categories: finite Toda theories (FTFTs), for which the underlying Kac–Moody algebra [1, 2] is a finite Lie algebra; affine Toda theories (ATFTs), for which the underlying Kac–Moody algebra is an affine algebra; and indefinite Toda theories (TTFTs), for which the underlying Kac–Moody algebra is an indefinite Kac–Moody algebra. The classes of FTFTs and ATFTs are well-studied and known to be integrable. In addition, the FTFTs enjoy conformal invariance. A review of the most interesting developments in ATFTs is presented in [3], where there is also a list of references to the original papers. The class of ITFTs is the least studied, as there are still many open questions regarding the indefinite Kac–Moody algebras. A special class of the ITFTs, namely the hyperbolic Toda theories (HTFTs), for which the underlying Kac–Moody algebra is a hyperbolic Kac–Moody algebra, were studied in [4], and it was shown that they are conformal but not integrable.

However, despite all progress in TFTs, there still remain many unresolved questions and problems. For example, one may ask what the structure constants of the conformally invariant TFTs are. In this paper, we address this question. We focus on FTFs and, in particular, on the A_2 FTT.

In section 2, the A_2 FTFT is introduced, some notations are fixed, and then we continue to show how the correlation function of exponential fields in the FTFT reduces to correlation functions of a free field theory with conformal W symmetry [5–8]. In section 3, we prove that, for some special cases of the exponential fields, the four-point correlation functions which contain a "degenerate" primary field satisfy the Riemann ordinary differential equation. Then, in section 4, the conformal bootstrap technique is applied to derive a set of functional equations for the structure constants of the A_2 FTFT.

2. A_2 Finite Toda field theory. We consider the finite conformal Toda field theory associated with the simply-laced Lie algebra A_2 described by the action

$$S = \int d^2x \left[\frac{1}{8\pi}(\partial\boldsymbol{\varphi})^2 + \mu \sum_{i=1}^{2} e^{b\mathbf{e}_i \cdot \boldsymbol{\varphi}} + \frac{R}{4\pi}\mathbf{Q} \cdot \boldsymbol{\varphi} \right]. \quad (1)$$

In this equation, $\mathbf{e}_i$ ($i = 1, 2$) are the simple roots of Lie algebra A_2. These define the fundamental weights $\mathbf{w}_i$ of the Lie algebra by the equation

$$\mathbf{e}_i \cdot \mathbf{w}_j = \delta_{ij}.$$

The background charge $\mathbf{Q}$ is proportional to the Weyl vector $\boldsymbol{\rho}$:

$$\mathbf{Q} = (b + 1/b)\boldsymbol{\rho}, \quad \boldsymbol{\rho} = \sum_{i=1}^{2} \mathbf{w}_i.$$

The local conformal invariance of the FTFT with central charge

$$c = 2 + 12\mathbf{Q}^2$$

---

is ensured by the existence of the holomorphic and anti-holomorphic energy–momentum tensors

$$T(z) = -\frac{1}{2}(\partial\boldsymbol{\varphi})^2 + \mathbf{Q}\cdot\partial^2\boldsymbol{\varphi},$$

$$\overline{T}(\bar{z}) = -\frac{1}{2}(\bar{\partial}\boldsymbol{\varphi})^2 + \mathbf{Q}\cdot\bar{\partial}^2\boldsymbol{\varphi}.$$

It is well known that the FTFTs possess, besides the standart conformal symmetry, an additional W symmetry. In particular, the A_2 FTFT we are studying in this paper contains the additional holomorphic and antiholomorphic currents $W(z)$ and $\overline{W}(\bar{z})$ with spin 3, which generate the W_3 algebra.

The vertex operators

$$V_{\mathbf{a}}(x) = e^{2\mathbf{a}\cdot\boldsymbol{\varphi}(x)}$$

are spinless primary fields of the W algebra. Let L_n and W_n be the Fourier modes of the holomorphic fields $T(z)$ and $W(z)$. Then

$$L_0 V_{\mathbf{a}} = \Delta(\mathbf{a})V_{\mathbf{a}}, \quad W_0 V_{\mathbf{a}} = w(\mathbf{a})V_{\mathbf{a}},$$

$$L_n V_{\mathbf{a}} = 0, \quad W_n V_{\mathbf{a}} = 0, \; n > 0,$$

where the conformal dimension $\Delta(\mathbf{a})$ is given by

$$\Delta(\mathbf{a}) = 2\mathbf{a}\cdot(\mathbf{Q} - \mathbf{a}).$$

The correlation function of N vertex operators is formally defined by the functional integral

$$G_{\mathbf{a}_1, \ldots, \mathbf{a}_n}(x_1, \ldots, x_n) = \int D\boldsymbol{\varphi}\prod_{i=1}^{N} e^{2\mathbf{a}_i\cdot\boldsymbol{\varphi}(x_i)}e^{-S[\boldsymbol{\varphi}]}. \quad (2)$$

We introduce the following orthogonal decomposition of the field φ

$$\boldsymbol{\varphi}(x) = \boldsymbol{\varphi}_0 + \tilde{\boldsymbol{\varphi}}(x),$$

where $\boldsymbol{\varphi}_0$ is the zero mode and $\tilde{\boldsymbol{\varphi}}$ denotes the part of the field that is orthogonal to the zero mode:

$$\int d^2 x \tilde{\boldsymbol{\varphi}}(x) = 0.$$

Now, the integration of the functional integral in Eq. (2) over zero mode $\boldsymbol{\varphi}_0$ can be done in a fashion similar to the Liouville case [9] to find

$$G_{\mathbf{a}_1, \ldots, \mathbf{a}_n}(x_1, \ldots, x_n) = \left(\frac{\mu}{8\pi}\right)^{s_1+s_2}\frac{1}{b^2|\det e|}\Gamma(-s_1)\Gamma(-s_2)$$

$$\times \int D\tilde{\boldsymbol{\varphi}}\prod_{i=1}^{N} e^{2\mathbf{a}_i\tilde{\boldsymbol{\varphi}}(x_i)}\left(\int d^2 x e^{b\mathbf{e}_1\cdot\tilde{\boldsymbol{\varphi}}}\right)^{s_1}\left(\int d^2 x e^{b\mathbf{e}_2\cdot\tilde{\boldsymbol{\varphi}}}\right)^{s_2}e^{-S_0[\tilde{\boldsymbol{\varphi}}]}, \quad (3)$$

where S_0 is the action of the free field theory,

$$S_0 = \int d^2 x\left(\frac{1}{8\pi}(\partial\tilde{\boldsymbol{\varphi}})^2 + \frac{R}{4\pi}\mathbf{Q}\cdot\tilde{\boldsymbol{\varphi}}\right),$$

and

$$s_1 = (b\det e_{ij})^{-1}[-Qe_{22} + k_1 e_{22} - k_2 e_{21}],$$

$$s_1 = (b\det e_{ij})^{-1}[-Qe_{12} + k_2 e_{11} - k_1 e_{12}],$$

$$\mathbf{k} = 2\sum_{i=1}^{N}\mathbf{a}_i, \quad \mathbf{Q} = (Q, 0).$$

Assuming that s_1 and s_2 both are positive integers, the remaining functional integral in Eq. (3) can be reduced to the correlation function of the W_3 minimal model [7, 8]. Unfortunately, the situation is much more complicated; i.e., in general, s_1 and s_2 are not positive integers. However, the solution to the problem is hidden in the previous observation; supposing that we know the exact expressions of the structure constants for the W_3 minimal model, we can recover the expressions for the structure constants of the A_2 FTFT by analytic continuation (similarly to the Liouville case) [10, 11].

3. Four-point correlation functions. Now, let us concentrate on the following four-point correlation function:

$$\langle V_{\mathbf{a}_+}(z)V_{\mathbf{a}_1}(z_1)V_{\mathbf{a}_2}(z_2)V_{\mathbf{a}_3}(z_3)\rangle = G_{\mathbf{a}_+\mathbf{a}_1\mathbf{a}_2\mathbf{a}_3}(z, z_1, z_2, z_3), \quad (4)$$

where the special vertex operator

$$V_{\mathbf{a}_+}(z) = e^{2\mathbf{a}_+\cdot\boldsymbol{\varphi}}, \quad \mathbf{a}_+ = (-b, b/\sqrt{3})$$

satisfies the null-vector equation

$$[\Delta_+(5\Delta_+ + 1)W_{-2}$$
$$-12w_+ L_{-1}^2 + 6w_+(\Delta_+ + 1)L_{-2}]V_{\mathbf{a}_+} = 0. \quad (5)$$

Taking into account the last equation and the explicit representation of the current W in terms of the field $\partial\boldsymbol{\varphi}$ (see [8]), we find that the selected four-point correlation function satisfies the differential equation

$$(\Delta_+ + 1)\frac{\partial^2}{\partial z^2}\langle V_{\mathbf{a}_+}(z)V_{\mathbf{a}_1}(z_1)V_{\mathbf{a}_2}(z_2)V_{\mathbf{a}_3}(z_3)\rangle$$

$$-2\sum_{i=1}^{3}\left[\frac{\Delta_i + \delta_i}{(z-z_i)^2} + \frac{1}{z-z_i}\frac{\partial}{\partial z_i}\right]$$

$$\times\langle V_{\mathbf{a}_+}(z)V_{\mathbf{a}_1}(z_1)V_{\mathbf{a}_2}(z_2)V_{\mathbf{a}_3}(z_3)\rangle \quad (6)$$

$$+4\sum_{i=1}^{3}\frac{A_i}{z-z_i}\langle V_{\mathbf{a}_+}\ldots\partial\varphi_1 V_{\mathbf{a}_i}\ldots\rangle$$

$$+4\sum_{i=1}^{3}\frac{B_i}{z-z_i}\langle V_{\mathbf{a}_+}\ldots\partial\varphi_2 V_{\mathbf{a}_i}\ldots\rangle = 0,$$

where

$$\delta_i = -2\sqrt{2}i[2a_{+2}(a_{i2}^2 - a_{i1}^2) + 2a_{i2}(a_{+1}^2 - a_{+2}^2)$$
$$+ a_{+2}a_{i1}(4a_{+1} - Q) - a_{+1}a_{i2}(4a_{i1} - Q)],$$

$$A_i = 2\sqrt{2}i(a_{+2}a_{i1} + a_{+1}a_{i2}),$$

$$B_i = 2\sqrt{2}i(a_{+1}a_{i1} - a_{+2}a_{i2}).$$

Moreover, for the special ratios

$$\frac{a_{i2}}{a_{i1}} = -\frac{a_{+2}}{a_{+1}} \pm \sqrt{1 + \left(\frac{a_{+2}}{a_{+1}}\right)^2} \qquad (7)$$

of the charges $\mathbf{a}_i$, Eq. (6) can be further reduced to the equation

$$(\Delta_+ + 1)\frac{\partial^2}{\partial z^2}\langle V_{\mathbf{a}_+}(z)V_{\mathbf{a}_1}(z_1)V_{\mathbf{a}_2}(z_2)V_{\mathbf{a}_3}(z_3)\rangle$$
$$- 2\sum_{i=1}^{3}\left[\frac{\Delta_i + \delta_i}{(z - z_i)^2} + \frac{1 + A}{(z - z_i)}\frac{\partial}{\partial z_i}\right] \qquad (8)$$
$$\times \langle V_{\mathbf{a}_+}(z)V_{\mathbf{a}_1}(z_1)V_{\mathbf{a}_2}(z_2)V_{\mathbf{a}_3}(z_3)\rangle = 0,$$

where $A = \pm 2\sqrt{2}\,i\sqrt{a_{+1}^2 + a_{+2}^2}$. It is well known that, in the case of four-point functions, the partial differential Eq. (8) can be reduced, using the projective Ward identities [12], to the Riemann ordinary differential equation

$$\left\{\frac{1}{2}(\Delta_+ + 1)\frac{d^2}{dz^2} + \sum_{i=1}^{3}\left[\frac{1 + A}{z - z_i}\frac{d}{dz} - \frac{\Delta_i + \delta_i}{(z - z_i)^2}\right]\right.$$
$$\left. + (1 + A)\sum_{i<j}^{3}\frac{\Delta_+ + \Delta_{ij}}{(z - z_i)(z - z_j)}\right\} \qquad (9)$$
$$\times \langle V_{\mathbf{a}_+}(z)V_{\mathbf{a}_1}(z_1)V_{\mathbf{a}_2}(z_2)V_{\mathbf{a}_3}(z_3)\rangle = 0,$$

where $\Delta_{ij} = \Delta_i + \Delta_j - \Delta_k$, $(k \neq i, j)$, $(i, j, k = 1, 2, 3)$.

4. Functional equations for structure constants. Now, any four-point function can be explicitly decomposed in terms of the three-point function

$$G_{\mathbf{a}_1\mathbf{a}_2\mathbf{a}_3\mathbf{a}_4}(z, \bar{z})$$
$$= \langle V_{\mathbf{a}_1}(z_1, \bar{z}_1)V_{\mathbf{a}_2}(z_2, \bar{z}_2)V_{\mathbf{a}_3}(z_3, \bar{z}_3)V_{\mathbf{a}_4}(z_4, \bar{z}_4)\rangle$$
$$= \sum_{\mathbf{a}}\mathbb{C}(\mathbf{a}_1, \mathbf{a}_2, \mathbf{Q} - \mathbf{a})\mathbb{C}(\mathbf{a}, \mathbf{a}_3, \mathbf{a}_4) \qquad (10)$$
$$\times \left|F_{\mathbf{a}}\begin{pmatrix} \mathbf{a}_1 & \mathbf{a}_2 \\ \mathbf{a}_3 & \mathbf{a}_4 \end{pmatrix}(z, \bar{z})\right|^2.$$

Conformal invariance allows us to set $z_1 = 0$, $z_2 = z$, $z_3 = 1$, and $z_4 = \infty$. As a consequence, the crossing symmetry condition is written as

$$G_{\mathbf{a}_1\mathbf{a}_2\mathbf{a}_3\mathbf{a}_4}(z, \bar{z}) = G_{\mathbf{a}_1\mathbf{a}_2\mathbf{a}_3\mathbf{a}_4}(1 - z, 1 - \bar{z})$$
$$= z^{-2\Delta_2}\bar{z}^{-2\bar{\Delta}_2}G_{\mathbf{a}_1\mathbf{a}_3\mathbf{a}_2\mathbf{a}_4}(1/z, 1/\bar{z}).$$

To gain additional information about the structure constants of the FTFT, we will use the technique suggested in [13]. So, let us assume that $\mathbf{a}_2 = \mathbf{a}_+$; i.e., correlation function (10) includes the degenerate field $V_{\mathbf{a}_+}$. Then the charges of the intermediate channel will take the following values [7]

$$(a_{11} + a_{+1}, a_{12} + a_{+2}),$$
$$(a_{11} - a_{+1}, a_{12} + a_{+2}), \quad (a_{11}, a_{12} - 2a_{+2}). \qquad (11)$$

This implies the following "fusion rules":

$$V_{\mathbf{a}_+}V_{\mathbf{a}} = [V_{a_1 + a_{+1}, a_2 + a_{+2}}]$$
$$+ [V_{a_1 - a_{+1}, a_2 + a_{+2}}] + [V_{a_1, a_2 - 2a_{+2}}].$$

It is more convenient to introduce the following "parametrization" of the intermediate charge (11):

$$\mathbf{a}(s) = (a_{11} + sa_{+1}, a_{12} + (3s^2 - 2)a_{+2}),$$
$$s = 0, \pm 1.$$

Using this parametrization, we can rewrite Eq. (10) as follows:

$$G_{\mathbf{a}_1\mathbf{a}_+\mathbf{a}_3\mathbf{a}_4}(z, \bar{z}) = \sum_{s = 0, \pm 1}\mathbb{C}(\mathbf{a}_1, \mathbf{a}_+, \mathbf{Q} - \mathbf{a}(s))$$
$$\times \mathbb{C}(\mathbf{a}(s), \mathbf{a}_3, \mathbf{a}_4)\left|F_s\begin{pmatrix} \mathbf{a}_1 & \mathbf{a}_+ \\ \mathbf{a}_3 & \mathbf{a}_4 \end{pmatrix}(z, \bar{z})\right|^2. \qquad (12)$$

In this notation, the crossing symmetry relation for $G_{\mathbf{a}_1\mathbf{a}_+\mathbf{a}_3\mathbf{a}_4}(z, \bar{z})$ is

$$\sum_{s = 0, \pm 1}\mathbb{C}_s(\mathbf{a}_1)\mathbb{C}(\mathbf{a}(s), \mathbf{a}_3, \mathbf{a}_4)\left|F_s\begin{pmatrix} \mathbf{a}_1 & \mathbf{a}_+ \\ \mathbf{a}_3 & \mathbf{a}_4 \end{pmatrix}(z, \bar{z})\right|^2$$

$$= |z|^{-4\Delta_2}\sum_{p = 0, \pm 1}\mathbb{C}_p(\mathbf{a}_4)\mathbb{C}(\mathbf{a}(p), \mathbf{a}_3, \mathbf{a}_1) \qquad (13)$$
$$\times \left|F_p\begin{pmatrix} \mathbf{a}_4 & \mathbf{a}_+ \\ \mathbf{a}_3 & \mathbf{a}_1 \end{pmatrix}(1/z, 1/\bar{z})\right|^2,$$

where we have denoted

$$\mathbb{C}(\mathbf{a}_1, \mathbf{a}_+, \mathbf{Q} - \mathbf{a}(s)) = \mathbb{C}_s(\mathbf{a}_1)$$

and

$$\mathbb{C}(\mathbf{a}_4, \mathbf{a}_+, \mathbf{Q} - \mathbf{a}(p)) = \mathbb{C}_p(\mathbf{a}_4).$$

It follows from Eq. (9) that the conformal block must satisfy the following relation:

$$
F_s \begin{pmatrix} \mathbf{a}_1 & \mathbf{a}_+ \\ \mathbf{a}_3 & \mathbf{a}_4 \end{pmatrix} (z, \bar{z}) = z^{-2\Delta_+}
$$

$$
\times \sum_{p = 0, \pm 1} M_{ps} F_p \begin{pmatrix} \mathbf{a}_4 & \mathbf{a}_+ \\ \mathbf{a}_3 & \mathbf{a}_1 \end{pmatrix} (1/z, 1/\bar{z}),
$$

(14)

where M_{ps} is a matrix that is determined by the monodromy properties of the differential Eq. (9) or, alternatively, can be determined by the method developed in [14]. The exact analytic expression of the matrix M_{ps} can be found in a number of papers [8, 15, 14]. We will not write down these expressions for the reason of the limited frame of the paper.

Substituting Eq. (14) into Eq. (13), we find the following functional equations for the A_2 FTFT structure constants:

$$
\sum_{s = 0, \pm 1} \mathbb{C}_s(\mathbf{a}_1) \mathbb{C}(\mathbf{a}(s), \mathbf{a}_3, \mathbf{a}_4) M_{s, 0} \overline{M}_{s, 1} = 0,
$$

$$
\sum_{s = 0, \pm 1} \mathbb{C}_s(\mathbf{a}_1) \mathbb{C}(\mathbf{a}(s), \mathbf{a}_3, \mathbf{a}_4) M_{s, 0} \overline{M}_{s, -1} = 0, \quad (15)
$$

$$
\sum_{s = 0, \pm 1} \mathbb{C}_s(\mathbf{a}_1) \mathbb{C}(\mathbf{a}(s), \mathbf{a}_3, \mathbf{a}_4) M_{s, 1} \overline{M}_{s, -1} = 0,
$$

provided that $\mathbf{a}_1$, $\mathbf{a}_3$, and $\mathbf{a}_4$ satisfy the constraint (7).

It is important to notice that Eq. (5) admits additional solutions besides $\mathbf{a}_+$. In particular, $\mathbf{a}^+ = (-b, -b\sqrt{3})$, $\mathbf{a}_- = (-1/b, 1/b\sqrt{3})$, and $\mathbf{a}^- = (-1/b, -1/b\sqrt{3})$ are all solutions to Eq. (5). Therefore, the set of Eqs. (15) should be complemented by a similar set of equations obtained for the special case $\mathbf{a}^+$ and then added for each "dual equation" using the substitutions $b \longrightarrow 1/b$ and $\mu \longrightarrow \tilde{\mu}$. The parameter $\tilde{\mu}$ is defined by the duality relations [16]

$$
\pi\mu\gamma\left(\frac{\mathbf{e}_i^2 b^2}{2}\right) = \pi\tilde{\mu}\gamma\left(\frac{2}{\mathbf{e}_i^2 b^2}\right)^{\mathbf{e}_i^2 b^2/2},
$$

where $\gamma(x) = \Gamma(x)/\Gamma(1 - x)$.

In principle, in terms of the special function "Upsilon" [10, 11], the complete set of the algebraic equations derived above for the special cases $\mathbf{a}_+$, $\mathbf{a}^+$, $\mathbf{a}_-$, and $\mathbf{a}^-$ allows the computation of all structure constants for the A_2 FTFT. We postpone the difficult problems of the exact determination of the structure constants and proof of the uniqueness of the solution for future studies.

REFERENCES

1. V. G. Kac, *Infinite Dimensional Algebras* (Cambridge Univ. Press, Cambridge, 1993, 3rd ed.).

2. P. Goddard and D. Olive, Int. J. Mod. Phys. A **1**, 303 (1986).

3. E. Corrigan, hep-th/9412213.

4. R. W. Gebert, T. Inami, and S. Mizoguchi, Int. J. Mod. Phys. A **11**, 5479 (1996).

5. A. Bilal, in *String Theory and Quantum Gravity: Proceedings of the Trieste Spring School, 1990*, Ed. by M. Green *et al.* (World Scientific, Singapore, 1991).

6. P. Bouwknegt and K. Schoutens, Phys. Rep. **223**, 183 (1993).

7. V. Fateev and A. Zamolodehikov, Nucl. Phys. B **280** [FS18], 644 (1987).

8. V. Fateev and S. Lukyanov, Sov. Sci. Rev., Sect. A **212**, 212 (1990).

9. M. Goulian and M. Li, Phys. Rev. Lett. **66**, 2051 (1991).

10. H. Dorn and H. Otto, Phys. Lett. B **291**, 39 (1992).

11. A. Zamolodchikov and Al. Zamolodchikov, Nucl. Phys. B **477**, 577 (1996).

12. A. Belavin, A. Polyakov, and A. Zamolodchikov, Nucl. Phys. B **241**, 333 (1984).

13. J. Teschner, Phys. Lett. B **363**, 65 (1995).

14. V. Dotsenko and V. Fateev, Nucl. Phys. B **240** [FS12], 312 (1984).

15. J. Teschner, hep-th/0104158.

16. C. Ahn, P. Baseilhac, V. Fateev, *et al.*, hep-th/0002213.

High-Energy Optical Schrödinger Solitons

V. N. Serkin[1, 2, *] and T. L. Belyaeva[2, 3]

[1] *Institute of General Physics, Russian Academy of Sciences, ul. Vavilova 38, Moscow, 117942 Russia*
* e-mail: vserkin@yahoo.com
[2] *Benemérita Universidad Autonoma de Puebla, Instituto de Ciencias, 72001 Puebla, Mexico*
[3] *Moscow State University, Vorob'evy gory, Moscow, 119899 Russia*
Received November 9, 2001

The conditions for the existence of a Lax pair were determined and exact analytic solutions to the nonlinear evolution equations of the Schrödinger type with complex and nonuniform potentials were found. In particular, these solutions provide a basis for the soliton management concept in applied problems and solve the problems of optimal energy accumulation by a Schrödinger soliton in an active medium and soliton amplification in optical fiber communication lines and soliton lasers. © 2001 MAIK "Nauka/Interperiodica".

PACS numbers: 42.65.Tg; 05.45.Yv

Optical solitons described by the nonlinear Schrödinger equation (NSE) are ideal carriers of an information bit [1–3]. Japanese firm NTT has already conducted pioneering experiments on information transmission by optical solitons in the Tokyo Metropolitan Network commercial optical fiber net operating in an ordinary (linear) mode with a rate of 2.4 Gbit/s. In the soliton mode, the rate of information transmission through this net was as high as 40 Gbit/s. Even more impressive results were achieved in laboratory conditions, where one succeeded in transmitting information with a rate very close to a terabit per second [2, 3].

The optimal amplification of optical solitons, i.e., an increase in the soliton energy with complete conservation of information bit and elastic character of their interaction, is one of the basic problems of fully optical soliton communication lines (where laser, rather than electronic, amplifiers are used as retransmitters).

It should be emphasized that, besides the applied importance in optical solitonics, the search for new integrable models and their soliton solutions is of general physical interest, because the soliton approach is universal in different fields of modern physics [4].

The problem of soliton amplification has a rather long history. After Zakharov and Shabat had proved in their pioneering works [5, 6] that the NSE is completely integrable and found canonical soliton solutions to this equation, Karpman *et al.* [7, 8] developed the adiabatic perturbation theory for solitons and demonstrated that the adiabatic amplification (or absorption) of solitons in the almost integrable systems is always accompanied by tail growing, which results in the loss of the elastic character of interaction between solitons in actual optical experiments [9]. The use of the inverse scattering method for the adequate analysis of nonlinear wave fields created during the amplification of optical soli-

tons showed [10] that energy increase in a soliton pulse is accompanied by an increase in the fraction of a nonsoliton radiation component. Moreover, in the nonadiabatic amplification regime, new extra solitons are created (see also experimental works cited in [9]). A solution to the problem of optimal soliton amplification has come to a deadlock; indeed, experiments on the generation of high-energy solitons are being conducted in homogeneous nonconservative systems, which are described by nonintegrable models. This fact basically rules out the possibility of amplifying a soliton as a whole with the conservation of its unique properties.

New solutions found in this work to the problem of amplifying optical solitons demonstrate that the "ideal" (both adiabatic and nonadiabatic) amplification of a soliton is really possible if the dispersion and nonlinear properties of a nonconservative system are specially controlled in an experiment.

Let us demonstrate that the problem of amplifying Schrödinger solitons in inhomogeneous and nonconservative systems is integrable (has the Lax representation) and find the conditions for the existence of its exact analytic solutions.

The method of the search for and solution to integrable nonlinear differential equations, named, after its authors, the Zakharov–Shabat [5, 6] and Ablowitz–Kaup–Newell–Segur [11] method of spectral problem, has become one of the important achievements in mathematical physics. Let us represent the desired nonlinear evolution equation as the condition for integrability of a pair of linear differential equations, to which the inverse scattering method can apply:

$$\frac{\partial \hat{L}}{\partial t} - \frac{\partial \hat{A}}{\partial x} + [\hat{L}, \hat{A}] = 0. \qquad (1)$$

This equation must be valid for all values of spectral parameter Λ and is known as the generalization of Lax representation (Lax pairs [12]) defining the set of equations for the scattering potential $q(x, t)$. Considering the general case of the time-dependent spectral parameter and taking matrices $\hat{L}$ and $\hat{A}$ in the form

$$\hat{L} = \begin{bmatrix} -i\Lambda(t) & \sqrt{R(t)/D(t)}\,q(x, t) \\ -\beta\sqrt{R(t)/D(t)}\,q^*(x, t) & i\Lambda(t) \end{bmatrix}, \tag{2}$$

$$\hat{A} = \begin{bmatrix} A & B \\ C & -A \end{bmatrix},$$

where

$$A = i$$
$$\times \left[\alpha(t)x - \frac{\beta}{2}R(t)|q(x, t)|^2 + \Gamma(t) + V(t)\Lambda + D(t)\Lambda^2 \right], \tag{3}$$

$$B = \sqrt{\frac{R(t)}{D(t)}}\left[-\frac{i}{2}D(t)\frac{\partial}{\partial x} - V(t) - D(t)\Lambda \right]q(x, t), \tag{4}$$

$$C = \beta\sqrt{\frac{R(t)}{D(t)}}\left[-\frac{i}{2}D(t)\frac{\partial}{\partial x} + V(t) + D(t)\Lambda \right]q^*(x, t), \tag{5}$$

one can easily verify that Eq. (1) generates the nonlinear evolution equation for the potential $q(x, t)$ of the form

$$i\frac{\partial q}{\partial t} = \frac{1}{2}D(t)\frac{\partial^2 q}{\partial x^2} + \beta R(t)|q|^2 q - 2\alpha(t)xq$$
$$+ \frac{i}{2}\frac{W[R(t), D(t)]}{R(t)D(t)}q - iV(t)\frac{\partial q}{\partial t} - 2\Gamma(t)q. \tag{6}$$

This equation has Lax representation (1)–(5) and differs from the canonical NSE [5, 6] by the presence, in addition to the spatiotemporal nonuniform potentials $\alpha(t)x$, $D(t)$, and $R(t)$, of the complex potential (gain coefficient)

$$iG(t) = \frac{i}{2}\frac{W[R(t), D(t)]}{R(t)D(t)}, \tag{7}$$

which is determined by the Wronskian $W[R(t), D(t)] = RD'_t - DR'_t$ of two arbitrary functions: dispersion $D(t)$ and nonlinearity $R(t)$.

Finally, the set of linear equations to be solved by the Zakharov–Shabat inverse scattering method has the form

$$\frac{\partial\psi_1(x, t)}{\partial x} = -i\Lambda\psi_1 + \sqrt{\frac{R(t)}{D(t)}}q(x, t)\psi_2,$$
$$\frac{\partial\psi_2(x, t)}{\partial x} = -\beta\sqrt{\frac{R(t)}{D(t)}}q^*(x, t)\psi_1 + i\Lambda\psi_2, \tag{8}$$

$$\frac{\partial\psi_1(x, t)}{\partial x} = i\left[\alpha(t)x + D(t)\Lambda^2 + V(t)\Lambda \right.$$
$$\left. -\frac{1}{2}\beta R(t)|q(x, t)|^2 + \Gamma(t) \right]\psi_1 - \sqrt{\frac{R(t)}{D(t)}}$$
$$\times \left[(D(t)\Lambda + V(t))q(x, t) + \frac{i}{2}D(t)\frac{\partial q(x, t)}{\partial x} \right]\psi_2,$$

$$\frac{\partial\psi_2(x, t)}{\partial t} = \beta\sqrt{\frac{R(t)}{D(t)}} \tag{9}$$
$$\times \left[(D(t)\Lambda + V(t))q^*(x, t) - \frac{i}{2}D(t)\frac{\partial q^*(x, t)}{\partial x} \right]\psi_1$$
$$+ i\left[-\alpha(t)x - D(t)\Lambda^2 - V(t)\Lambda \right.$$
$$\left. + \frac{1}{2}\beta R(t)|q(x, t)|^2 - \Gamma(t) \right]\psi_2.$$

For the canonical case of constant coefficients $D(t) = R(t) = 1$ and spectral parameter $\partial\Lambda/\partial t = \alpha(t) = \alpha_0 = $ const, Eq. (6) is greatly simplified and takes the form of the NSE for an Alfvén wave in an inhomogeneous plasma [13]:

$$i\frac{\partial q}{\partial t} = \frac{1}{2}\frac{\partial^2 q}{\partial x^2} + |q|^2 q - 2\alpha_0 xq. \tag{10}$$

Historically, particle-like solutions to Eq. (10) were first obtained by Chen and Liu [13] and were the first example of the generalization of the Zakharov–Shabat problem to the case of a time-dependent spectral parameter. The solutions found to Eq. (10) substantially extended the notion of a soliton and generalized it to the accelerated motion of a soliton in an external potential and its reflection from the potential.

In our case of variable and linearly independent coefficients (7), the solution to Eq. (6) displays one more new property of a soliton: solitons not only can be accelerated but they can also be amplified, remaining "true" solitons (conserving the elastic character of interaction upon energy accumulation).

We illustrate new possibilities by an example of the amplification of optical solitons. The transition to the problems of optical solitonics is accomplished in Eqs. (1)–(10) by the substitution [9]

$$q(x, t) \longrightarrow \widetilde{\Psi^\pm}(Z, X); \quad x \longrightarrow X;$$
$$t \longrightarrow Z; \quad X = (t - Z/v)/\tau_0,$$

where τ_0 is the initial pulse duration; Z is the spatial coordinate normalized to the characteristic length of dispersive pulse smearing; and X is the dimensionless time in the frame of reference moving with the group

velocity for pulse solitons, or it is the transverse coordinate for spatial beam solitons. The function $\widetilde{\Psi^\pm}(Z, X)$ is the dimensionless complex wave-packet envelope.

In practical applications, the following completely integrable models are of primary interest for the amplification of optical solitons in inhomogeneous systems.

(i) The basic equation

$$i\frac{\partial\widetilde{\Psi^\pm}}{\partial Z} = \pm\frac{1}{2}D(Z)\frac{\partial^2\widetilde{\Psi^\pm}}{\partial X^2} + \beta R(Z)\left|\widetilde{\Psi^\pm}\right|^2\widetilde{\Psi^\pm}$$
$$+ \frac{i}{2}\frac{W[R(Z), D(Z)]}{R(Z)D(Z)}\widetilde{\Psi^\pm}. \qquad (11)$$

(ii) The equations derived from Eq. (11) and describing the energy accumulation by a soliton at an arbitrary gain $G(Z)$:

$$i\frac{\partial\widetilde{\Psi^\pm}}{\partial Z} = \pm\frac{1}{2}\Phi(Z)\exp\left\{-2\gamma_0 Z + 2\int_0^Z G(\zeta)d\zeta\right\}\frac{\partial^2\widetilde{\Psi^\pm}}{\partial X^2} \quad (12)$$
$$+ \beta\Phi(Z)\left|\widetilde{\Psi^\pm}\right|^2\widetilde{\Psi^\pm} - i\gamma_0\widetilde{\Psi^\pm} + iG(Z)\widetilde{\Psi^\pm};$$

$$i\frac{\partial\widetilde{\Psi^\pm}}{\partial Z} = \pm\frac{1}{2}F(Z)\frac{\partial^2\widetilde{\Psi^\pm}}{\partial X^2} + \beta F(Z)$$
$$\qquad\qquad\qquad\qquad\qquad (13)$$
$$\times\exp\left\{2\gamma_0 Z - 2\int_0^Z G(\zeta)d\zeta\right\}\left|\widetilde{\Psi^\pm}\right|^2\widetilde{\Psi^\pm} - i\gamma_0\widetilde{\Psi^\pm} + iG(Z)\widetilde{\Psi^\pm},$$

where the functions $G(Z)$, $R(Z)$, $D(Z)$, $\Phi(Z)$, and $F(Z)$ are arbitrary once integrable and differentiable real functions.

Analytic solutions to Eq. (11) for so-called fundamental bright and dark (at rest) solitons have the form

$$\Psi^\pm(Z, X) = \sqrt{\frac{D(Z)}{\beta R(Z)}}$$

$$\times\begin{bmatrix}\eta\,\text{sech}(\eta X)\exp\left\{-0.5i\eta^2\int_0^Z D(\zeta)d\zeta\right\} \\[2em] \eta\,\tanh(\eta X)\exp\left\{-i\eta^2\int_0^Z D(\zeta)d\zeta\right\}\end{bmatrix}. \qquad (14)$$

Let us consider some particular examples.

(i) Nonlinear tunneling of a Schrödinger soliton through a solitary amplification (absorption) line. We represent complex potential $iG(Z)$ (7) in Eq. (11) in the form of a solitary amplification line, e.g., as

$$G(Z) = g + \text{sech}^2[\delta(Z - Z_0)], \qquad (15)$$

where the parameter g accounts for linear losses in the

system. This model is completely integrable if the function $D(Z)$ (referred below to as the dispersion control function) has the form

$$D(Z)$$
$$= \exp\left\{-2gZ + \frac{2}{\delta}\left[\frac{\sinh(\delta Z)}{\cosh[\delta(Z - Z_0)]\cosh(\delta Z_0)}\right]\right\}. \qquad (16)$$

The dynamics of soliton amplification in the parametric region (15) and (16) is shown in Fig. 1. The process of soliton amplification is nontrivial, because the potential jump $G(Z)$ (15) necessitates the corresponding jump in $D(Z)$ (16) even in the absence of linear radiation losses in the system.

The soliton amplification process becomes even more interesting in the presence of nonzero linear losses in the system. It follows from Eq. (16) that there is a g value for which a soliton initially damped in the line completely recovers its parameters (see Fig. 1).

(ii) Nonlinear tunneling of a Schrödinger soliton through dispersion (or nonlinear) wells and barriers. Let us represent the real function $D(Z)$ [or $R(Z)$] in the form of a solitary potential barrier, e.g.,

$$D(Z) = 1 + \varepsilon\,\text{sech}^2[\delta(Z - Z_0)]. \qquad (17)$$

In this case, model (11) is completely integrable if the complex potential $iG(Z)$ has the form of Eq. (7), where

$$G(Z)$$
$$= -\frac{\varepsilon\delta\,\text{sech}^2[\delta(Z - Z_0)]\tanh[\delta(Z - Z_0)]}{\{1 + \varepsilon\,\text{sech}^2[\delta(Z - Z_0)]\}}. \qquad (18)$$

The dynamics of soliton tunneling through dispersion barrier (17) is shown in Fig. 2.

Thus, there are completely integrable generalized NSE models for the amplification of Schrödinger solitons (11)–(18). Computer simulation with a great variety of functions satisfying the condition for complete integrability of model (11) corroborates the conclusion that interaction between the resulting solutions is elastic. Figure 3 presents a typical example of elastic interaction between Schrödinger solitons during the amplification.

The found Lax representation and the exact analytic solutions for model (11) provide a theoretical basis for the idea of soliton management [14, 15]. Indeed, as follows from Eqs. (11)–(13), any change in some parameter of a soliton system (this may be a soliton communication line or a soliton laser) requires the appropriate correction of the other parameters. A change in only one parameter, e.g., the periodic sign alternation for the dispersion parameter $D(Z)$ in a system with so-called fiber dispersion management [2, 3], leads to the loss of complete integrability by a soliton system. In this connection, the recommendations justified in [16] for the designers of soliton communication lines are of fundamental importance. The solutions found in this work
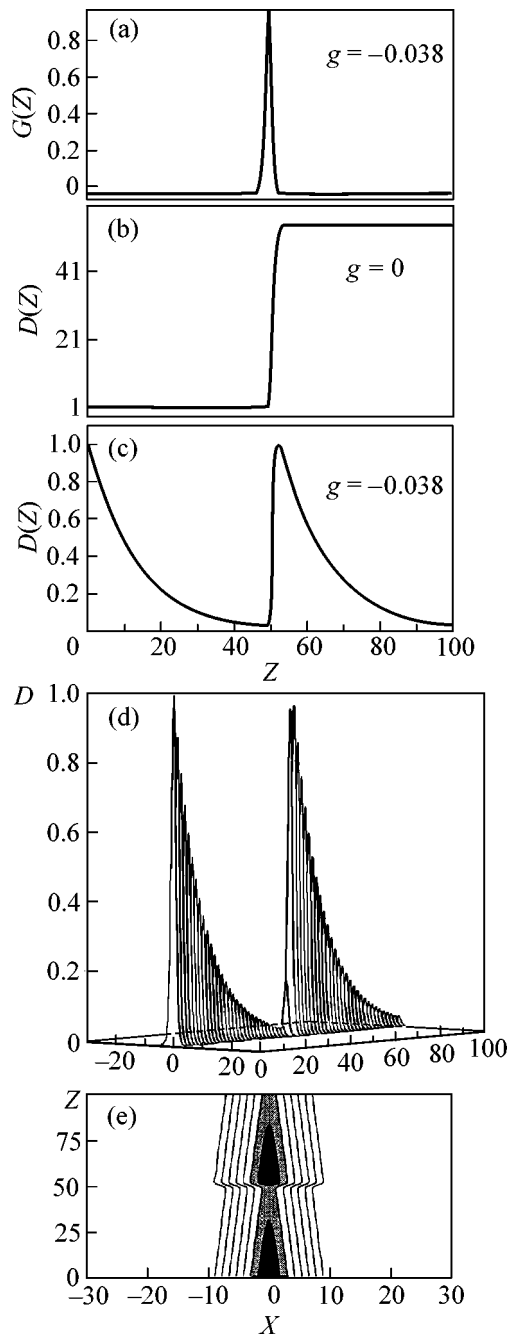
Fig. 1. Nonlinear tunneling of a Schrödinger soliton through potential barrier (15) (solitary amplification line): (a)–(c) the gain $G(Z)$ and the corresponding dispersion parameter $D(Z)$ as functions of length Z for $R(Z) = 1$, $Z_0 = 50$, $\delta = 1.0$, and $g = 0$ and -0.038; (d) and (e) demonstrate the formation of a high-energy soliton in parametric region (15) and (16) for $R(Z) = 1$, $Z_0 = 50$, $\delta = 1.0$, and $g = -0.038$; and (e) logarithmic contour map for soliton intensity $I = 0.1$, 0.01, ∞.

Fig. 2. Nonlinear tunneling of a Schrödinger soliton through the solitary dispersion barrier (17): (a) the potential barrier shape $D(Z)$ and the corresponding potential $G(Z)$ as functions of length Z for $\varepsilon = 2.0$, $\delta = 1.0$, $Z_0 = 5$, and $R(Z) = 1$; and (b) spatiotemporal dynamics of a soliton pulse. Lower panel: equipotential curves for $D = 1, 0.1, \infty$.

differ cardinally from [14, 15] in that their experimental implementation does not require any initial frequency modulation for a soliton pulse, whereas the solutions obtained in [14, 15] exist only in the presence of this
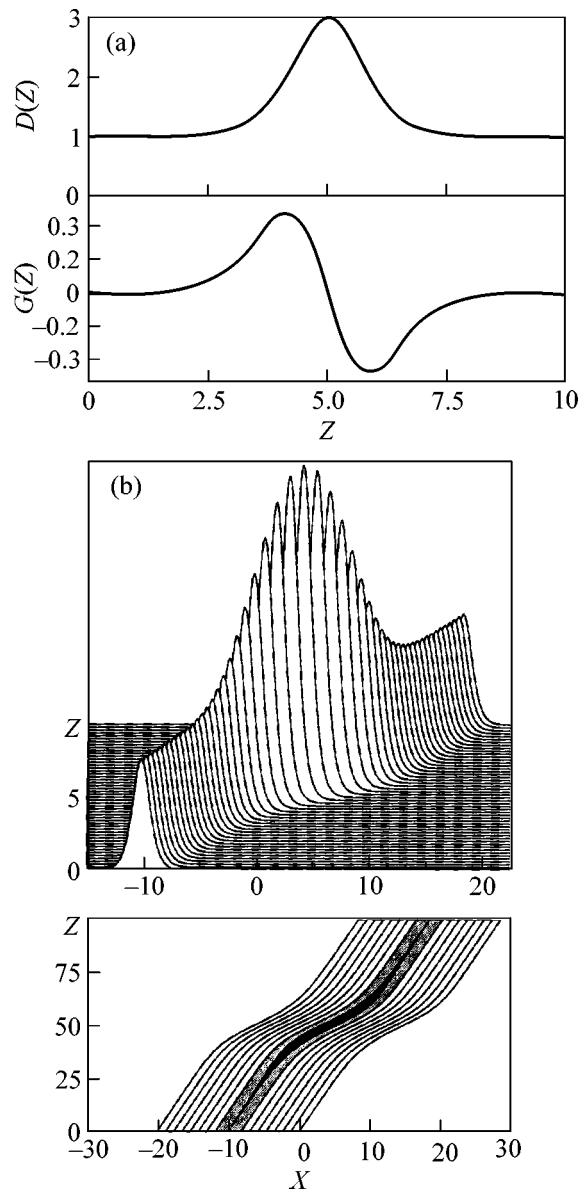
modulation, the latter being uniquely related to the duration and amplitude of the soliton pulse, which vary following the spatial variations of phase modulation of the channeled radiation.

In addition, the specificity of the aforementioned phenomena of Schrödinger soliton nonlinear tunneling through the complex (amplifying) potentials and generation of high-energy solitons is that the soliton duration remains constant in the course of energy accumulation. This fact is highly important for soliton communication lines [2, 3].
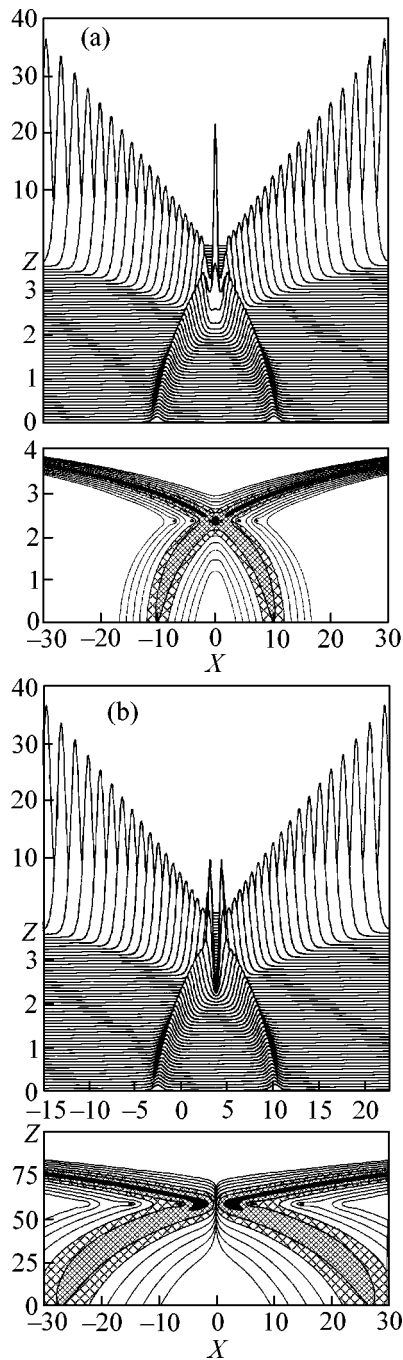
A solution to the problem of optimal amplification of optical solitons is presented in this work in a very general form and enables one to easily choose the optimal relations between the functions $D(Z)$, $R(Z)$, and $G(Z)$ for each particular experiment. The determination of fundamental parameters, such as the limiting energy and duration of a soliton in active laser systems, requires additional investigations based, e.g., on the direct methods of solving the set of nonlinear Maxwell equations [17]. In conclusion, we emphasize that Lax representation (1)–(5) and model (6) are not uniquely possible. More complicated completely integrable models of soliton amplification will be discussed elsewhere.

REFERENCES

1. L. F. Mollenauer, R. G. Stolen, and J. R. Gordon, Phys. Rev. Lett. **45**, 1095 (1980).
2. *Massive WDM and TDM Soliton Transmission Systems: A ROSC Symposium*, Ed. by Akira Hasegawa (Kluwer, Boston, 2000).
3. M. Nakazawa, H. Kubota, K. Suzuki, *et al.*, Chaos **10**, 486 (2000).
4. J. A. Krumhansl, Phys. Today **44** (3), 33 (1991).
5. V. E. Zakharov and A. B. Shabat, Zh. Éksp. Teor. Fiz. **61**, 118 (1971) [Sov. Phys. JETP **34**, 62 (1972)].
6. V. E. Zakharov and A. B. Shabat, Zh. Éksp. Teor. Fiz. **64**, 1627 (1973) [Sov. Phys. JETP **37**, 823 (1973)].
7. V. I. Karpman and E. M. Maslov, Zh. Éksp. Teor. Fiz. **75**, 504 (1978) [Sov. Phys. JETP **48**, 252 (1978)].
8. V. I. Karpman and V. V. Solov'ev, Physica D (Amsterdam) **3**, 483 (1981).
9. *Optical Solitons–Theory and Experiment*, Ed. J. R. Taylor (Cambridge Univ. Press, Cambridge, 1992).
10. V. V. Afanasjev, V. N. Serkin, and V. A. Vysloukh, Sov. Lightwave Commun. **2**, 35 (1992).
11. M. J. Ablowitz, D. J. Kaup, A. C. Newell, and H. Segur, Stud. Appl. Math. **53**, 249 (1974).
12. P. D. Lax, Commun. Pure Appl. Math. **21**, 467 (1968).
13. H. H. Chen and C. S. Liu, Phys. Rev. Lett. **37**, 693 (1976).
14. V. N. Serkin and A. Hasegawa, Phys. Rev. Lett. **85**, 4502 (2000).
15. V. N. Serkin and A. Hasegawa, Pis'ma Zh. Éksp. Teor. Fiz. **72**, 125 (2000) [JETP Lett. **72**, 89 (2000)].
16. V. E. Zakharov and S. V. Manakov, Pis'ma Zh. Éksp. Teor. Fiz. **70**, 573 (1999) [JETP Lett. **70**, 578 (1999)].
17. V. N. Serkin, É. M. Shmidt, T. L. Belyaeva, and S. N. Khotyaintsev, Dokl. Akad. Nauk **359**, 760 (1998) [Dokl. Phys. **43**, 206 (1998)].

Fig. 3. Nonlinear interaction dynamics between (a) in-phase and (b) antiphase high-energy solitons $\tilde{\Psi}(Z, X) =$

$$\exp(G_0 Z)\eta \, \text{sech}(\eta X) \, \exp\left\{ -\frac{i\eta^2}{4G_0}[\exp(2G_0 Z) - 1] \right\} \quad \text{for}$$

the model $i\dfrac{\partial \tilde{\Psi}}{\partial Z} = \dfrac{1}{2}\exp(2G_0 Z)\dfrac{\partial^2 \tilde{\Psi}}{\partial X^2} + |\tilde{\Psi}|^2 \tilde{\Psi} + iG_0 \tilde{\Psi}$

with $G_0 = 1.0$, $\eta = 1.0$, and group velocity detuning $\Delta V = 2.0$ ($V_1 = -V_2 = -1.0$). The logarithmic contour map for soliton intensity $l = 10, 1, 0.1, \infty$ are shown.

Translated by R. Tyapaev

Theoretical Treatment and Simulation of New UV Crystal CsLiB$_6$O$_{10}$ in Third-Harmonic Generation[1]

L. Wang* and S. Chen

Department of Physics, Hebei Normal University, Shijiazhuang 050016, P.R.China
*e-mail: Lwang.1@yeah.net
Received November 5, 2001

We calculated theoretically the properties of the nonlinear crystal CsLiB$_6$O$_{10}$ (CLBO) in third-harmonic generation (THG). These are the phase matching angle, the effective nonlinear coefficient, the walk-off angle, the permitted angle, and the permitted wavelength, and we found that CLBO has a small walk-off angle and large permitted parameters, as compared with BBO. The numerical simulation curves of the conversion efficiency were obtained for the case where CLBO was used in THG of a *Q*-switched Nd:YAG laser with a wavelength of 1064 nm and different pump powers and the optimized efficiency was as high as 22%. All this suggests that the CLBO crystal is more suitable for generating intense higher order harmonic radiation. © *2001 MAIK "Nauka/Interperiodica".*

PACS numbers: 42.65.Ky

1. INTRODUCTION

The exploration of a solid ultraviolet (UV) laser is important because of its high power and small volume; it was the pioneer of UV lasers on the latest nonlinear crystal CsLiB$_6$O$_{10}$ (CLBO) [1, 2]. However, their shortest transparent band is always very broad; for example, the shortest transparent band of BBO is 190 nm and 175 nm in CLBO [3, 4] and also has high damage threshold and many other beneficial optical properties. This work on CLBO concerns its SHG and third-harmonic generation (THG) in a picosecond (ps) or nanosecond (ns) Nd:YAG laser with a fundamental wavelength of 1064 nm in experiment; there is no report on its properties in the theory, especially on its THG. In this paper, we calculated and numerically simulated theoretical curves for its phase-matching (PM) angle, effective nonlinear coefficient, walk-off angle, permitted angle and wavelength, and conversion efficiency of CLBO in THG and determined where it has a smaller walk-off angle, broader permitted parameters, and high conversion efficiency on UV; all this proved that CLBO is more suitable to produce higher-order radiation of high power, and we present its prospect as a high-power UV solid laser.

2. COMPUTER SIMULATION OF PERMITTED PARAMETERS FOR CLBO

Taking the collinear interaction into consideration, we supposed that ω_1 (λ_1) and ω_2 (λ_2) were the frequencies (wavelengths) of incident radiation, ω_3 (λ_3)

denoted frequency (wavelength) of the third-harmonic wave, and ω_1 was lower than ω_2, both of which were lower than ω_3.

2.1. PM angle (θ):

(A) PM angle of type I ($o + o \longrightarrow e$). According to the momentum and energy conservation laws, we can obtain

$$n_1(\omega_1) + 2n_2(\omega_2) = 3n_3(\omega_3, \theta), \quad (1)$$

$$\omega_1 = \omega_2/2 = \omega_3/3. \quad (2)$$

Where n_1, n_2, and n_3 are the reflection indices of the three waves. From Eqs. (1) and (2), the PM angle (θ) of THG in type I could be derived:

$$\theta(\mathrm{I}) = \arcsin\left(\frac{\dfrac{9n_0^2(\omega_3)n_e^2(\omega_3)}{[n_1(\omega_1) + 2n_2(\omega_2)]^2} - n_e^2(\omega_3)}{n_o^2(\omega_3) - n_e^2(\omega_3)} \right)^{1/2}. \quad (3)$$

(B) PM angle of type II ($e + o \longrightarrow e$). We define the type-II(l) PM in THG as follows: $o + e \longrightarrow e$ means that the radiation with frequencies ω_1 and ω_2 have *e* and *o* polarizations, respectively; and the other was type II(2), $o + e \longrightarrow e$, where the waves ω_1 and ω_2 were *o*- and *e*-polarized lights, respectively. The θ of type II(l)

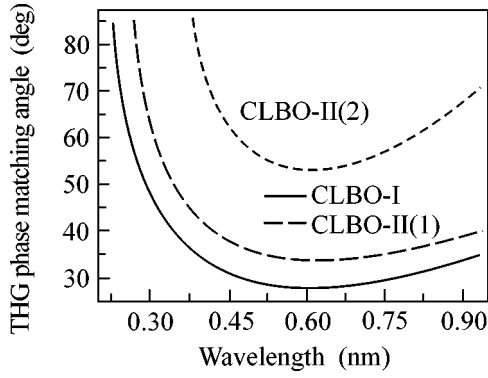
[1] This work was submitted by the authors in English.

Fig. 1. Curves of the phase-matching angle versus wavelength of the third harmonic radiation of different-type THG for the CLBO crystal.
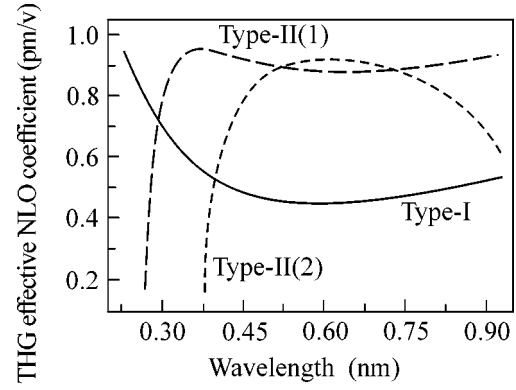
Fig. 2. Curves of the effective nonlinear coefficient versus the wavelength of the third-harmonic wave for THG of the CLBO crystal.
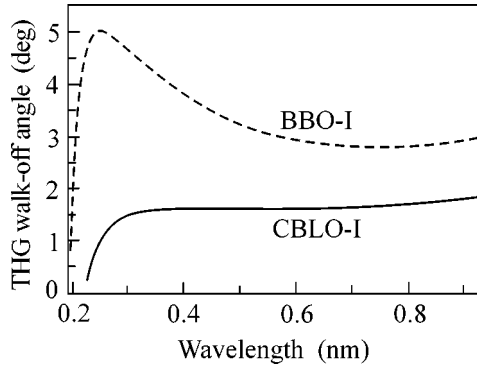
Fig. 3. THG walk-off angle curves of type-I phase matching for CLBO and BBO.
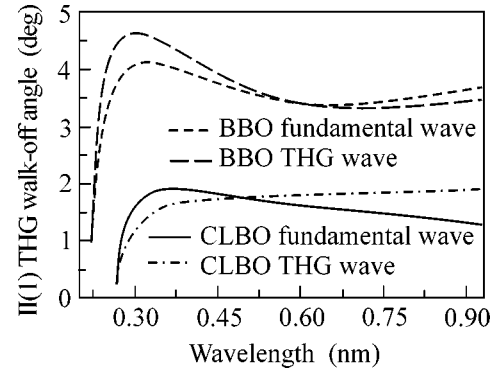
Fig. 4. THG walk-off angle curves of type-II(1) phase matching for CLBO and BBO.

and type II(2) in THG were written as

$$
3\left[\frac{\cos^2\theta(II(1))}{n_0^2(\omega_3)} + \frac{\sin^2\theta(II(1))}{n_e^2(\omega_3)}\right]^{-1/2}
$$

$$
= 2n_0(\omega_2) + \left[\frac{\cos^2\theta(II(1))}{n_o^2(\omega_1)} + \frac{\sin^2\theta(II(1))}{n_e^2(\omega_1)}\right]^{-1/2}, \quad (4)
$$

$$
3\left[\frac{\cos^2\theta(II(2))}{n_0^2(\omega_3)} + \frac{\sin^2\theta(II(2))}{n_e^2(\omega_3)}\right]^{-1/2}
$$

$$
= n_0(\omega_1) + 2\left[\frac{\cos^2\theta(II(2))}{n_o^2(\omega_2)} + \frac{\sin^2\theta(II(2))}{n_e^2(\omega_2)}\right]^{-1/2}. \quad (5)
$$

From Eqs. (3), (4), (5), and the sellimier equations of CLBO [1]

$$
n_{o(\lambda)}^2 = 2.2145 + \frac{0.00890}{\lambda^2 - 0.02051} - 0.01413\lambda^2, \quad (6)
$$

$$
n_{e(\lambda)}^2 = 2.0588 + \frac{000866}{\lambda^2 - 0.01202} - 0.006073\lambda^2. \quad (7)
$$

We were able to get the θ of CLBO in THG. The curves of CLBO's θ versus the THG wavelength are shown in Fig. 1, where we can see that the shortest wavelength of the CLBO's THG is 277 nm if CLBO is used as the type-I PM, and θ is 85°. The range of the λ_3 wave is the broadest in the type-I THG, where θ varies from about 25° to 85°, and the range is the shortest in the type-II(2) PM, where θ varies from 55° to 85°. It is also seen in Fig. 1 that there is no PM angle in type-II THG of CLBO if the wavelength λ_1 lies between 680 and 800 nm, and the type-I PM must be utilized. It is necessary that the crystal has a large birefringence in the type-II(2) THG, otherwise it is seldom used in practice [5].

2.2. Effective nonlinear coefficient (d_{eff})

CLBO is a negative uniaxial crystal with space group $\bar{4}2m$, and we can derive its d_{eff} by considering

the Kleinman equation [6]:

$$d_{\text{eff}}(\text{I}) \,=\, d_{36}\sin\theta\sin(2\phi), \qquad (8)$$

$$d_{\text{eff}}(\text{II}) \,=\, d_{36}\sin2\theta\cos(2\phi), \qquad (9)$$

where θ and ϕ are the orientation angle of CLBO. It is supposed that ϕ is 45° and 0° in type-I and type-II THG, respectively, and θ is inserted in Eqs. (8) and (9) using Fig. 1; at the same time, d_{36} is taken to be 0.95 pm/V [1]. Then, we can obtain the d_{eff} curves versus the wavelength ω_3 of CLBO in THG, as was shown in Fig. 2. In Fig. 2, the optimized d_{eff} is 0.95 pm/V when the wavelength ω_3 is 227 and 377 nm in type-I and type-II(l), respectively.

2.3. Walk-off angle (α)

The formula for the walk-off angle [7] is

$$\alpha \,=\, \tan^{-1}\left[\frac{1}{2}\frac{(n_e^2(\lambda)-n_o^2(\lambda))}{n_o^2(\lambda)\sin^2\theta+n_e^2(\lambda)\cos^2\theta}\sin(2\theta)\right], \quad (10)$$

where θ is the angle in Fig. 1. Considering Eqs. (6) and (7), we insert θ of the corresponding PM in Fig. 1 into Eq. (10) and then get the curves for the walk-off angle of CLBO in type-I, type-II(l), and type-II(2) THG. They are shown in Figs. 3–5, where BBO's walk-off angles are obtained in the same way, and the x axis is the wavelength ω_3 between 227 and 933 nm. From Figs. 3–5, we can find that the walk-off angles of CLBO are all much smaller than the ones of BBO under the same conditions.

2.4. Permitted parameters

(A) Permitted angle ($\Delta\theta$). The permitted angle $\Delta\theta$ of CLBO in THG of different PM state is as follows:

$$\Delta\theta \,=\, \pm\left|\frac{\pi/l}{\dfrac{\omega}{c}n_e^3(\omega_3,\theta)[n_e^{-2}(\omega_3)-n_o^{-2}(\omega_3)]\sin(2\theta)}\right|l, \qquad (11)$$

$$\Delta\theta(\text{II}(1)) \,=\, \pm\left|\frac{\pi/l}{\dfrac{\omega_3}{2c}n_e^3(\omega_3,\theta)[n_e^{-2}(\omega_3)-n_o^{-2}(\omega_3)]\sin(2\theta)+\dfrac{\omega_1}{2c}n_e^3(\omega_1,\theta)[n_e^{-2}(\omega_1)-n_o^{-2}(\omega_1)]\sin(2\theta)}\right|l, \quad (12)$$

$$\Delta\theta(\text{II}(2)) \,=\, \pm\left|\frac{\pi/l}{\dfrac{\omega_3}{2c}n_e^3(\omega_3,\theta)[n_e^{-2}(\omega_3)-n_o^{-2}(\omega_3)]\sin(2\theta)-\dfrac{\omega_2}{2c}n_e^3(\omega_2,\theta)[n_e^{-2}(\omega_2)-n_o^{-2}(\omega_2)]\sin(2\theta)}\right|l. \quad (13)$$

As long as θ is inserted from Fig. 1 into Eqs. (11), (12), and (13), the curves for the permitted angles are obtained versus the wavelength ω_3 ranging from 227 to 933 nm in type-I, type-II(l), and type-II(2) of CLBO in BM THG, as shown in Fig. 6; also, the corresponding BBO's permitted angles are presented, where we suppose that the crystal length of I is 10 mm. In Fig. 6, we find that the permitted angles of CLBO for any kind of

PM are broader than the ones in BBO in the corresponding state in THG; especially, when type II(2) is taken, the permitted angle $\Delta\theta$ of CLBO is as large as 65.6 mrad mm and that of BBO is only 4.42 mrad mm.

(B) Permitted wavelength ($\Delta\lambda$). The permitted wavelength $\Delta\lambda$ of CLBO in THG of each kind of PM should be written as

$$\Delta\lambda_1(\text{I}) \,=\, \pm\left|\frac{\lambda_1^2/l}{6\left[\dfrac{dn_e(\lambda_3,\theta)}{d\lambda_3}\lambda_3-n_e(\lambda_3,\theta)\right]-4\left[\dfrac{dn_o(\lambda_2)}{d\lambda_2}\lambda_2-n_0(\lambda_2)\right]-2\left[\dfrac{dn_o(\lambda_1)}{d\lambda_1}\lambda_1-n_o(\lambda_1)\right]}\right|l, \qquad (14)$$

$$\Delta\lambda_1(\text{II}(1)) \,=\, \pm\left|\frac{\lambda_1^2/l}{6\left[\dfrac{dn_e(\lambda_3,\theta)}{d\lambda_3}\lambda_3-n_e(\lambda_3,\theta)\right]-2\left[\dfrac{dn_e(\lambda_1,\theta)}{d\lambda_1}\lambda_1-n_e(\lambda_1,\theta)\right]-4\left[\dfrac{dn_o(\lambda_2)}{d\lambda_2}\lambda_2-n_o(\lambda_2)\right]}\right|l, \qquad (15)$$

$$\Delta\lambda_1(\text{II}(2)) \,=\, \pm\left|\frac{\lambda_1^2/l}{6\left[\dfrac{dn_e(\lambda_3,\theta)}{d\lambda_3}\lambda_3-n_e(\lambda_3,\theta)\right]-2\left[\dfrac{dn_e(\lambda_2,\theta)}{d\lambda_2}\lambda_2-n_e(\lambda_2,\theta)\right]-2\left[\dfrac{dn_o(\lambda_1)}{d\lambda_1}\lambda_1-n_o(\lambda_1)\right]}\right|l. \qquad (16)$$
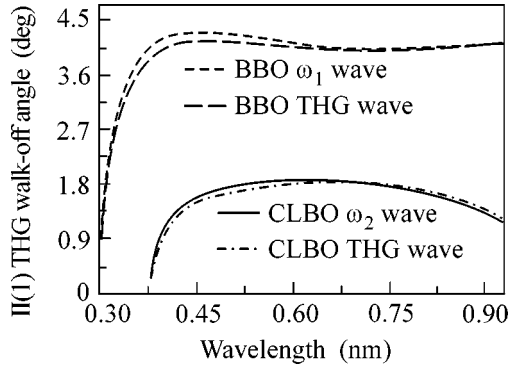
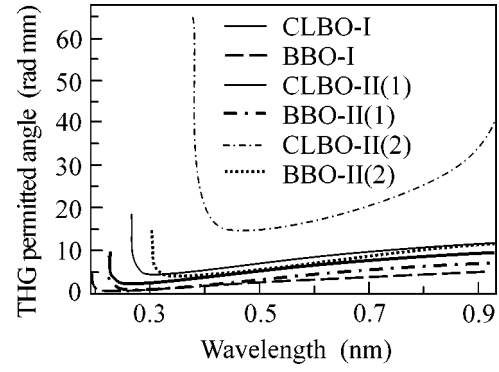**Fig. 5.** THG walk-off angle curves of type-II(2) phase-matching THG for CLBO and BBO.

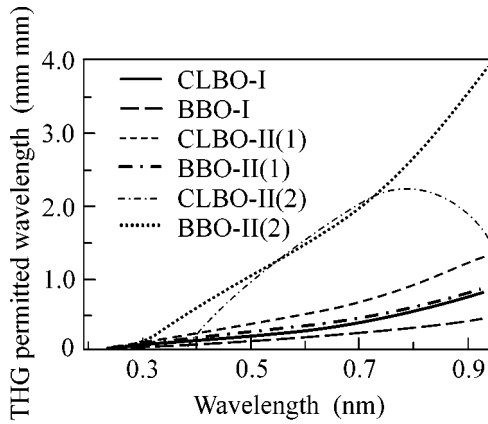**Fig. 6.** THG permitted angle curves for CLBO and BBO versus the wavelength of third-harmonic generation.

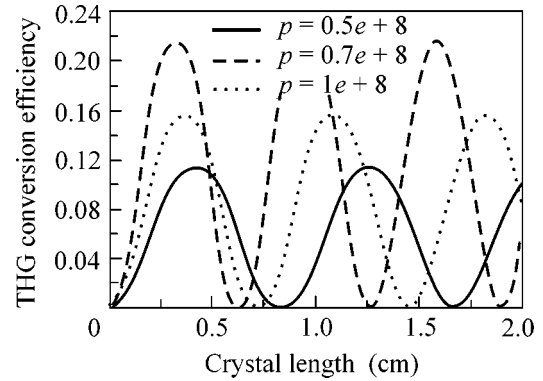**Fig. 7.** Permitted wavelength curves for CLBO and BBO crystals in THG.

Fig. 8. THG conversion efficiency of type II(l) for different intensities pumped in PM.

The crystal length l is also taken to be 10 mm, and we can obtain the curves for the CLBO's and BBO's permitted wavelengths according to Eqs. (14), (15), and (16) in a similar way of working out $\Delta\theta$ as shown in Fig. 7, where the x axis is the wavelength ω_3 ranging from 227 to 933 nm in the THG. From Fig. 7, we find that, when the wavelength ω_3 was between 330 and 933 nm, the CLBO's permitted wavelength of type-I and type-II(2) THG is larger than those of BBO.

It is shown in the curves from Fig. 3 to Fig. 7 that, in the THG of CLBO, the walk-off angle is smaller and the permitted parameters such as permitted angles and permitted wavelength are larger; this helps the CLBO in generating a high-order high-quality harmonic.

2.5. Conversion efficiency

When the incident wave is of the shape of a plane and the walk-off effect is ignored, the THG efficiency in CLBO is

$$\eta = \frac{\omega_3 t^2}{\omega_1 + \omega_2 t^2} \mathrm{sn}^2\left(\sqrt{\frac{1}{\omega_1 + t^2 \omega_2}} Dz, t\right) t < 1, \quad (17)$$

$$\eta = \frac{\omega_3 t'^2}{\omega_2 + \omega_1 t'^2} \mathrm{sn}^2\left(\sqrt{\frac{1}{\omega_2 + 't^2 \omega_1}} Dz, t'\right) t' < 1, \quad (18)$$

$$D = \left(\frac{16\pi^3 d_{\mathrm{eff}}^2 I_s}{n_1 n_2 n_3 \lambda_1 \lambda_2 \lambda_3 \varepsilon_0}\right)^{1/2}. \quad (19)$$

If it is defined that E_{20} and E_{10} are the original electric vectors, we can obtain

$$t = \sqrt{\frac{n_2}{2n_1}} \frac{E_{20}}{E_{10}},$$

$t' = I/t$; at the same time, $\mathrm{sn}(x, y)$ is the first kind Jacobi elliptic function; I_s is the incident intensity; and n_1, n_2, and n_3 are the refractive indices of the waves with frequencies of ω_1, ω_2, and ω_3, respectively.

We have simulated the conversion efficiency for CLBO's type-II(l) PM in THG, when the pumping light is a fundamental wave of 1064 nm in a Q-switched Nd:YAG laser. The first CLBO crystal was for SHG of type I with a length of 0.7 cm, and it was tuned to $\varphi = 45°$ and $\theta = 28.7°$; the second CLBO crystal was for THG of type II(l), and its θ and φ were 48.3° and 0°, respectively. Then, we find from [7] and in Fig. 2 that d_{eff} of the two crystals should be 0.46 and 0.94 pm/v, respectively. It is supposed for the second crystal that one of the pumping waves, $E_1(z)$, has a wavelength of 1064 nm, its refractive index n_1 is 1.4568, and its walk-off angle is 0.03 rad; the other, $E_2(z)$, has a wavelength of 532 nm, and it is o light with the refractive index n_2 equal to 1.4981. So we calculated that the THG, $E_3(z)$ has the refractive index n_3 of 1.4844, and its walk-off angle is 0.028 rad. From above, it is obvious that the walk-off effect in the CLBO is much smaller and we can take it for granted that Eqs. (17), (18), and (19) are suitable for THG of CLBO.

We obtained $D = 1.745 \times 10^4 \sqrt{I_s}$ according to Eq. (19); it was supposed that the beam diameter is that of the incident wave, and we simulated the curves for conversion efficiency versus length of the second crystal for a total pumping power P of 1×10^8 W, 0.7×10^8 W, and 0.5×10^8 W as is shown in Fig. 8. From Fig. 8, we can see that for P of 1×10^8 W, the optimized efficiency is as high as 22% in THG of CLBO, and when the incident intensity increases, the THG efficiency is enhanced, provided the crystal has the appropriate length. The damage threshold of CLBO is as high as 26 GW/cm² at 1064 nm, and its volume can be very large, which can provide an effective way to enhance the THG efficiency in CLBO.

As for the CLBO crystal, the walk-off angle is smaller and the permitted parameter is larger, which makes it possible to produce high-quality radiation of the third- or even a higher-order harmonic radiation in CLBO. The CLBO delivered higher THG conversion efficiency and better output stability than BBO at optimized crystal lengths. If CLBO is pumped by a Q-switched Nd:YAG laser with a beam diameter of 8 amm and a power of 1×10^8 W, the THG efficiency in CLBO can be 22%. At the same time, its damage threshold is high, from which we may speculate that, in the future, it will be used intensively in high-power solid UV lasers very.

REFERENCES

1. Y. Mori, I. Kuroda, S. Nakajima, *et al.*, Appl. Phys. Lett. **67**, 1818 (1995).
2. Y. K. Yap, M. Inagaki, S. Nakajima, *et al.*, Opt. Lett. **21**, 1348 (1996).
3. N. Umemura and K. Kato, Appl. Opt. **36**, 6794 (1997).
4. J. Y. Zhang, J. Y. Huang, Y. R. Shen, *et al.*, J. Opt. Soc. Am. B **10**, 1758 (1993).
5. Y. K. Yap, S. Naramura, A. Taguchi, *et al.*, Opt. Commun. **145**, 101 (1998).
6. D. Eimerk, L. Davis, S. Velsko, *et al.*, J. Appl. Phys. **62**, 1968 (1987).
7. Y. Mori, I. Kuroda, S. Nakajima, *et al.*, Jpn. J. Appl. Phys. **34** (3A), L296 (1995).

Measurement of the Boundary Frequency of the Inertial Interval of Capillary Wave Turbulence at the Surface of Liquid Hydrogen

M. Yu. Brazhnikov, G. V. Kolmakov, A. A. Levchenko*, and L. P. Mezhov-Deglin

Institute of Solid State Physics, Russian Academy of Sciences, Chernogolovka, Moscow region, 142432 Russia
*e-mail: levch@issp.ac.ru

The boundary frequency was experimentally measured for the upper edge of an inertial interval corresponding to the Kolmogorov spectrum for energy distribution over the oscillation frequencies at the surface of liquid hydrogen. It is shown that the dependence of boundary frequency ω_b on the wave amplitude η_p at the pump frequency ω_p is well described by the power law $\omega_b \sim \eta_p^{4/3} \omega_p^{23/9}$. © 2001 MAIK "Nauka/Interperiodica".

PACS numbers: 68.03.Kn; 47.35.+i; 47.27.Gs

It was shown, within the framework of the wave turbulence theory, that a system of nonlinear interacting waves at the surface of a fluid can be described by the kinetic equation analogous to the Boltzmann equation in gas dynamics [1]. In a system of capillary waves, there is a frequency interval (inertial interval) which is bounded from below by the pump frequency ω_p and from above by the frequency at which the viscous damping time τ_v is comparable, by an order of magnitude, to the nonlinear interaction time τ_n: $1/\tau_v \sim 1/\tau_n$.

The dispersion law for capillary waves $\omega = (\sigma/\rho)^{1/2} \kappa^{3/2}$ (ω is frequency, κ is the wave vector, σ is the surface tension, and ρ is density) is of the decay type, and, hence, the main contribution to the wave interaction comes from the three-wave processes of wave decay into two waves with the conservation of the total wave vector and frequency, as well as from the reverse processes of two-wave confluence into a single wave. Therefore, a constant energy flux to higher frequencies is established in the capillary-wave turbulence regime; hence, it occurs at frequencies higher than the pump frequency (direct cascade).

It is known [2] that the viscous damping time of capillary waves decreases with an increasing wave vector as

$$1/\tau_v = 2\nu\kappa^2, \qquad (1)$$

where ν is the kinematic viscosity of the fluid.

The nonlinear interaction characteristic time τ_n is determined by the fluid parameters and the capillary-wave distribution $n(\kappa)$ over the wave vector. It is written as

$$1/\tau_n \sim |V_{\kappa\kappa\kappa}|^2 n(\kappa)\kappa^2/\omega_\kappa, \qquad (2)$$

where $V_{\kappa\kappa\kappa} \approx (\sigma/\rho^3)^{1/4}\kappa^{9/4}$ is the three-wave nonlinear interaction constant and ω_κ is the frequency of the wave with vector κ.

The steady-state distribution of surface waves in the inertial interval can be described by the Fourier transform of the pair correlation function $I_\kappa = \langle |\eta_\kappa|^2 \rangle$ for the surface deviations $\eta(r, t)$ from the flat state. The correlation function is related to the distribution function $n(\kappa)$ by the expression

$$I_\kappa = n(\kappa)/\sigma^{1/4}\kappa^{1/2}. \qquad (3)$$

Equations (1)–(3) can be used to find the wave frequency ω_b, at which the viscous damping time and the nonlinear interaction time become comparable with each other by an order of magnitude, as a function of the wave amplitude η_p at pump frequency (boundary frequency at the upper edge of inertial interval)

$$\omega_b \sim \eta_p^\beta \omega_p^\gamma. \qquad (4)$$

The exponents β and γ are determined by the distribution function $n(\kappa) \sim (\kappa/\kappa_p)^\alpha$, where κ_p is the wave vector of the wave at pump frequency ω_p. For the excitation of surface oscillations in a broad frequency range, the exponent α of the distribution function is $-19/4$ [3], $\beta = 2.4$, and $\gamma = 19/5$. For the excitation of surface oscillations by a spectrally narrow pumping, $\alpha = -23/4$ [4], β decreases to $4/3$, and $\gamma = 23/9$.

The purpose of this work was to experimentally observe the boundary frequency at the upper edge of the inertial interval and study it as a function of the wave amplitude at pump frequency, as well as to compare the results with theoretical predictions.

EXPERIMENTAL

Experiments were carried out in an optical cell placed in a helium cryostat. A flat capacitor, with a radioactive platelet on its lower plate, was mounted horizontally inside the cell. Hydrogen was condensed into a container formed by the lower plate and a guard ring 25 mm in diameter and 3 mm in height. The liquid layer was 3 mm thick. The upper capacitor plate (collector with a diameter of 25 mm) was situated at a distance of 4 mm above the liquid surface. The liquid temperature in the experiments was maintained at 15 K.

The free fluid surface was charged by β electrons emitted from the radioactive platelet. Electrons ionized a thin liquid layer near the platelet. A dc voltage was applied to the capacitor plates. The sign of charges forming a quasi-two-dimensional layer underneath the liquid surface was controlled by the voltage polarity. In the experiments, the oscillations of a positively charged surface were studied. The metallic guard ring installed around the radioactive platelet prevented escape of charges from under the surface to the container walls. The surface oscillations of liquid hydrogen (standing waves) were excited at one of the resonance frequen-

Fig. 1. The P_ω^2 distribution for two wave amplitudes at a pump frequency of 135 Hz. Wave amplitudes: (a) 0.0045 and (b) 0.016 mm.

cies using an ac voltage applied to the guard ring additionally to the dc voltage.

Surface oscillations of liquid hydrogen were detected from the variations in the power of a laser beam reflected from the surface. The reflected beam was focused by a lens onto a photodetector. The voltage at the photodetector was directly proportional to the beam power $P(t)$ and recorded during several seconds on a computer interfaced to a high-speed 12- or 16-bit analog-to-digital converter. The frequency spectrum P_ω of the total reflected power was obtained by the temporal Fourier transform of the recorded $P(t)$ dependence.

In the experiments, a broad laser beam with a diameter of 0.5 mm was incident on the surface at a glancing angle of approximately 0.2 rad. The elliptic axes of the light spot at the surface were equal to 2.5 and 0.5 mm. It was pointed out in [5] that the squared amplitude of Fourier transform P_ω^2 of the measured signal is directly proportional to the correlation function in the frequency representation; i.e., $I_\omega \propto P_\omega^2$.

The methods of exciting surface oscillations, their recording, and experimental data processing are described in more detail in [6].

It was shown in the preliminary experiments that the wave amplitude at pump frequency depends linearly on the applied ac voltage. Because of this, after the cell was filled with hydrogen at a constant voltage between the capacitor plates, measurements were carried out on the maximal ac voltage at which the angle of beam deviation was equal to the known maximal value (until the upper capacitor plate was touched). At smaller amplitudes of ac voltage, the angle of deviation and the wave amplitude η were calculated from the experimental data.

RESULTS AND DISCUSSION

Figure 1 demonstrates two types of frequency dependences for the squared amplitude of Fourier transform P_ω^2 of the signal $P(t)$ measured at the surface excitation frequency $\omega_p = 135$ Hz. In Fig. 1a, the wave amplitude at the pump frequency is 0.0045 ± 0.0006 mm, and in Fig. 1b it is equal to 0.016 ± 0.009 mm. The frequencies at which the P_ω^2 function sharply changes (inertial interval) are indicated by the arrows. In Fig. 1a, the boundary frequency of the inertial interval edge is $\omega_b = 900 \pm 200$ Hz, and, in Fig. 1b, $\omega_b = 4500 \pm 400$ Hz. One can see that this frequency undergoes a high-frequency shift as the wave amplitude increases.

It follows from Fig. 1 that, at small wave amplitudes, the inertial interval is not too broad and involves a cascade consisting only of a few high-frequency harmonics of the pump frequency ω_p. At larger amplitudes, the inertial interval broadens and the cascade involves
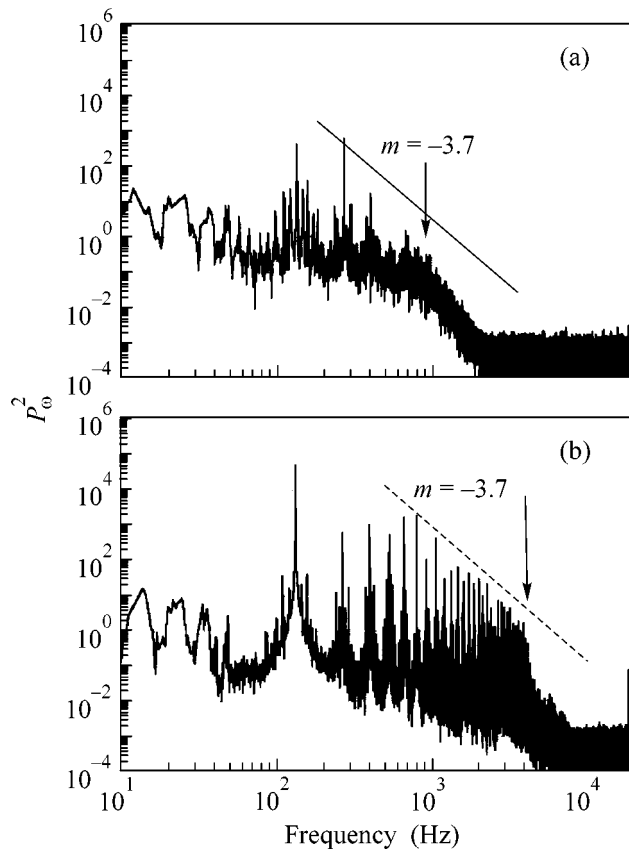
tens and hundreds of harmonics. Over a wide frequency range, the P_ω^2 dependence shows a power-law behavior with exponent $m = -3.7 \pm 0.3$. To illustrate this fact, a power function ω^m with exponent $m = -3.7$ is shown in Fig. 1b by the dotted line. This exponent is close to the estimate obtained in the theoretical work [4] for the case of spectrally narrow pumping. Numerical calculations show that the cascade I_ω represents a sequence of equidistant peaks at frequencies multiple of the pump frequency. The peak heights are described by the power function with an exponent of $-21/6$. This value differs by $4/6$ from the exponent found in [3] for the broadband pumping.

The boundary frequency of the inertial interval edge is shown in Fig. 2a as a function of wave amplitude for two pump frequencies, 83 and 135 Hz. The abscissas (frequencies) of the points in this figure were estimated from the experimental graphs analogous to those shown in Fig. 1. The point ordinates (pumping wave amplitudes) were calculated from the known amplitudes of the ac voltage applied to the guard ring. The solid lines in Fig. 2 correspond to the power-law dependence of the boundary frequency ω_b of the inertial interval on the amplitude η with an exponent of $4/3$. For better fit of the theoretical curve to the experimental data, Eq. (4) was supplemented by the constant term Ω which was independent of the wave amplitude at pump frequency. It is clear from simple physical considerations that the boundary frequency ω_b cannot be lower than the pump frequency ω_p. The results of the curve-fitting procedure is demonstrated in Fig. 2a. One can see that the agreement between the experimental points and the theoretical dependence is quite satisfactory. The constant term proved to be larger than the pump frequency ω_p by a factor of 2 or 3.

The dependence of the boundary frequency ω_b on the amplitude in Eq. (4) implies the presence of a scaling law with respect to the pump frequency. One can readily see that, irrespective of the pump frequency ω_p, all experimental points ω_b fall on a single straight line in the $\omega_b/\omega_p^{23/9}$, $\eta^{4/3}$ coordinates. The experimental data constructed with these coordinates are shown in Fig. 2b. One can state that the experimental points fall on a straight line for both pump frequencies. This confirms the validity of Eq. (4) as well as the results of calculating the capillary-wave distribution function for narrow-band pumping.

In summary, it is demonstrated experimentally that the inertial interval corresponding to the power-law frequency dependence of a correlation function is extended to higher frequencies as the wave amplitude at pump frequency rises. This dependence is well described by the power-law behavior with an exponent of $4/3$. The experimental results are in qualitative agreement with the conclusions of work [4].
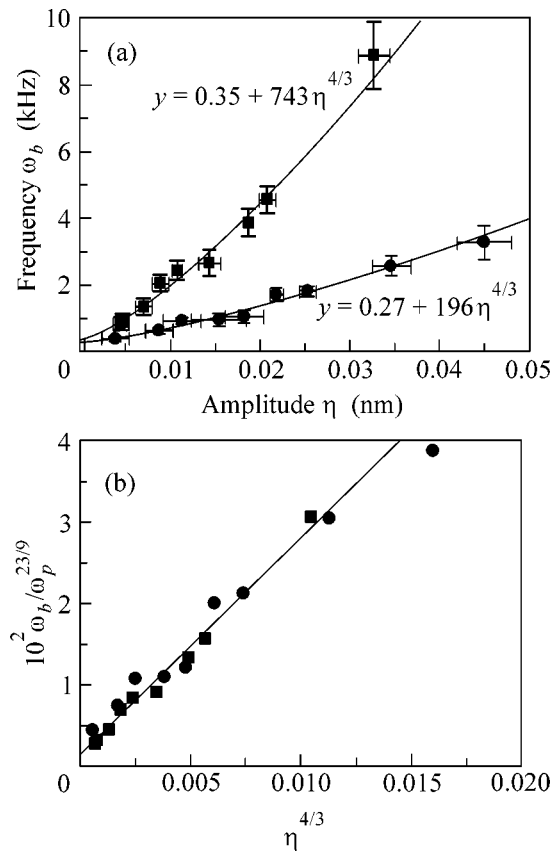
Fig. 2. Boundary frequency as a function of wave amplitude at pump frequencies of ($\bullet$) 83 and ($\blacksquare$) 135 Hz; (a) linear coordinates and (b) reduced coordinates.

REFERENCES

1. V. Zakharov, V. L'vov, and G. Falkovich, *Wave Turbulence*, Vol. 1: *Kolmogorov Spectra of Turbulence* (Springer-Verlag, Berlin, 1992).

2. L. D. Landau and E. M. Lifshitz, *Course of Theoretical Physics*, Vol. 6: *Fluid Mechanics* (Nauka, Moscow, 1988; Pergamon, New York, 1987).

3. V. E. Zakharov and N. N. Filonenko, Zh. Prikl. Mekh. Tekh. Fiz. **5**, 62 (1967).

4. G. E. Fal'kovich and A. B. Shafarenko, Zh. Éksp. Teor. Fiz. **94** (7), 172 (1988) [Sov. Phys. JETP **67**, 1393 (1988)].

5. M. Yu. Brazhnikov, A. A. Levchenko, G. V. Kolmakov, and L. P. Mezhov-Deglin, Fiz. Nizk. Temp. **27**, 1183 (2001).

6. M. Yu. Brazhnikov and A. A. Levchenko, Prib. Tekh. Éksp. (in press).

Translated by V. Sakun

Pion Production under the Action of Intense Ultrashort Laser Pulse on a Solid Target

V. Yu. Bychenkov[1], *, Y. Sentoku[2], S. V. Bulanov[3], K. Mima[2], G. Mourou[4], and S. V. Tolokonnikov[5]

[1] Lebedev Physical Institute, Russian Academy of Sciences, Leninskiĭ pr. 53, Moscow, 119991 Russia
*e-mail: bychenk@sci.lebedev.ru
[2] Institute of Laser Engineering, University of Osaka, 565-0871 Osaka, Japan
[3] Institute of General Physics, Russian Academy of Sciences, ul. Vavilova 38, Moscow, 119991 Russia
[4] Center for Ultrafast Optical Science, University of Michigan, 48109-2099 Ann Arbor, Michigan, USA
[5] Kurchatov Institute Russian Research Centre, pl. Kurchatova 1, Moscow, 123182 Russia
Received October 22, 2001; in final form November 14, 2001

Two-dimensional "particle-in-cell" modeling was carried out to determine the laser intensity threshold for pion production by protons accelerated by the relativistically strong short laser pulses acting on a solid target. The pion production yield was determined as a function of laser intensity. © *2001 MAIK "Nauka/Interperiodica".*

PACS numbers: 52.38.Kd; 25.40.Qa

Generation of energetic ions by ultrashort laser pulses interacting with plasma has been the object of active studies over recent years [1–9]. This is primarily dictated by the necessity of understanding the mechanisms of ion acceleration as a result of the interaction of laser radiation with plasma, including the quantitative description of the characteristics of these mechanisms. The problem of ion acceleration is among the key problems in various applications of high-power lasers such as fast ignition for laser fusion, injection of fast particles, and fabrication of radioactive sources in medicine and nuclear physics. Due to the effective acceleration of ions in a laser field, they can initiate nuclear reactions.

At the present level of energies, ultrashort pulsed lasers are capable of initiating various nuclear reactions, such as nuclear fusion, fission, pickup, stripping, charge-transfer, and radiative capture [1]. Nuclear reactions in the collisions of laser-accelerated ions with a nuclear target were observed experimentally at energies from several MeV to tens of MeV [5–7]. The detection of protons with an energy of 60 MeV at a laser intensity of 3×10^{20} W/cm² [5] and the progress in laser energy buildup allow one to assume that the pion-production threshold of 140 MeV will be surmounted in the near future. The generation of such energies in the laboratory, rather than on accelerators, may have a profound effect on the priorities in laser technology and nuclear research techniques. With these prospects in mind, it is profitable to estimate quantitatively the pion yield as a function of laser parameters and determine the corresponding laser intensity threshold. In this communication, the results of relativistic two-dimensional particle-in-cell (PIC) modeling are presented.

Note that the pion production by a short laser pulse and the pion yield have already been discussed in [10]. This process was associated with the formation of gamma-ray quanta, which initiated pion photoproduction. The formation of gamma-ray quanta is caused by the bremsstrahlung of laser-accelerated electrons, after which gamma-ray quanta interact with nuclei to produce Δ isobars that decay with pion emission. This transformation chain is highly inefficient because of its electromagnetic nature, as contrasted to the strong interactions of protons and nuclei discussed below.

In our computations, we modeled the interaction of a short 300-fs linearly polarized pulse with a solid 5-μm-thick foil representing a uniform plasma layer with a density forty times higher than its critical value. Laser radiation with a wavelength of 1 μm was incident normally to the foil surface and propagated along the X direction of the modeling plane XY of size 50×10 μm. The focusing spot size was 3 μm, and the computations were carried out for several values of laser intensity I in the range from 2×10^{20} to 5×10^{21} W/cm², which corresponded to a relativistically strong laser field $a \gg 1$, where $a = eA/mc^2$ is the amplitude of the normalized vector potential A, and c, e, and m are the light velocity, the electron charge, and the electron mass, respectively. For definiteness, a two-component plasma composed of 50% H and 50% D was considered. To make the model as realistic as possible, a 30-μm-thick layer of rarefied plasma was placed ahead of the foil, and its density was taken to be constant and equal to 10^{21} cm⁻³. The point is that the laser pulse is nonideal and preceded by a prepulse at experimental power levels much higher than 1 TW, leading to the appearance of a rather extended

40-μm-thick "preplasma" layer at the target surface before the pulse peak reaches it [5]. Such a underdense plasma strongly affects the character of interaction between the pulse and the target. The plasma proved to be nontransparent for intensities $I \lesssim 5 \times 10^{21}$ W/cm². We also carried out the computations for an intensity of 1.2×10^{22} W/cm², for which the relativistic transparency effect arose and a substantial fraction of laser radiation passed through the target.

The preplasma electrons with relativistic energies are accelerated in the forward direction, pass through the thin foil, and create a strong ion-accelerating electrostatic field. The formation of the ion-accelerating electric field is a rather complicated process, because the generation of quasi-static magnetic fields and the formation of a region with an excess of positive electric charge may play an important role in this case [11]. Without going into details (see [11]), note that it is the generation of hot electrons which is at the origin of the ion acceleration. For the relativistic intensities, the main part of the laser energy transforms into the energy of hot electrons [5, 12]. Then the kinetic energy T_h of hot electrons transforms into the energy of electrostatic field accelerating ions. Accordingly, one should expect that the energy ϵ_i of the latter is on the order of the energy of hot electrons; i.e., $\epsilon_i \sim ZT_h$. Our computations suggest that, indeed, the characteristic proton energy varies in proportion to the temperature of hot electrons with changing laser intensity. The deuteron acceleration is suppressed appreciably, as compared to the proton acceleration. Due to higher mobility, protons are accelerated first, as a result of which the electric field behind them decreases and less efficiently accelerates deuterons following them. As a result, the calculated deuteron energy did not exceed one-fourth of the proton energy. This effect was observed experimentally in [7], where the proton and deuteron energies were equal to 9 and 2 MeV, respectively.

When passing through the preplasma, laser radiation was canalized, due to the relativistic self-focusing effect, to efficiently accelerate electrons. Qualitatively, their energy distribution corresponded to the Maxwell distribution with temperature T_h satisfying approximately a root law $T_h \propto \sqrt{I}$ with respect to the laser intensity. At the same time, the electron motion proves to be highly complicated (stochastic) because of the complex structure of the fields, including the reflected laser wave and the fields generated in plasma. The behavior $\propto \sqrt{I}$ of the hot electron temperature corresponds qualitatively to the scaling law for the electron energy accumulation in a relativistically strong electromagnetic wave propagating in plasma with the phase velocity ω/k higher than the light velocity $ck \lesssim \omega$. The dependence of the dimensionless electron kinetic energy γ on the laser intensity in the ultrarelativistic limit $a \gg 1$ can be estimated using the well-known inte-

grals of motion [13] for an electron in an electromagnetic field,

$$\frac{p_x}{mc} = \frac{ck}{\omega}\gamma, \quad \frac{p_y}{mc} = a, \quad \gamma = \sqrt{\frac{p_x^2}{m^2c^2} + \frac{p_y^2}{m^2c^2}}, \quad (1)$$

which are written for an initially quiescent electron. According to Eq. (1), $\gamma = a\omega/\sqrt{\omega^2 - c^2k^2} \propto \sqrt{I}$. This scaling law is similar to the one obtained from the ponderomotive potential [14] $T_h = mc^2(\sqrt{1 + a^2} - 1) \simeq mc^2a$. However, contrary to the latter, it includes a contribution from the longitudinal electron momentum, which is not smaller than the transverse momentum and, hence, adds to the energy. This is confirmed by our computations showing that the formula for T_h from [14] underestimates the temperature of hot electrons.

We studied the ion energy as a function of laser intensity in the absence of preplasma and established that this dependence was also close to the root law, as in the case with preplasma, but the energy was slightly lower. Therefore, the presence of preplasma is quite important, because it enhances the generation efficiency of both fast electrons and ions. In Fig. 1, the energy spectra of the forward accelerated protons are shown for three values of laser intensity $I \leq 5 \times 10^{21}$ W/cm². As the energy increases, the high-energy tail shown in this figure transforms into a plateaulike distribution with an abrupt cutoff. Such a plateaulike distribution with energy cutoff was observed experimentally in [4–7, 15], and it is typical of the electrostatic ion-acceleration mechanism. The cutoff corresponds to the maximal potential difference created by hot electrons. At a higher intensity of 1.2×10^{22} W/cm², plasma becomes relativistically transparent, and the inductive electric field arising on the rear side of the target due to the generated magnetic field plays a substantial part in the ion acceleration [16].

Evidently, once the cutoff in the proton spectrum exceeds 140 MeV, protons can produce π^+ in a sub-
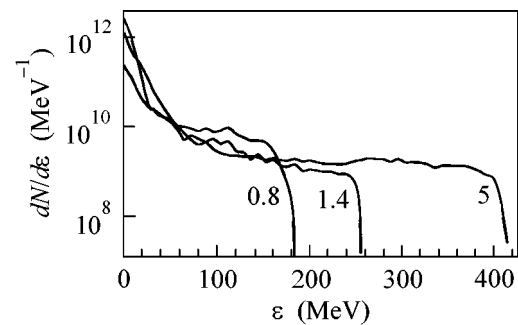

Fig. 1. Energy distribution of the number of forward accelerated protons at different laser intensities I. The values of I in 10^{21} W/cm² are indicated near the corresponding curves.
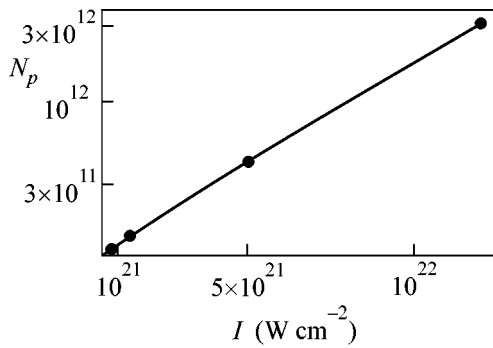
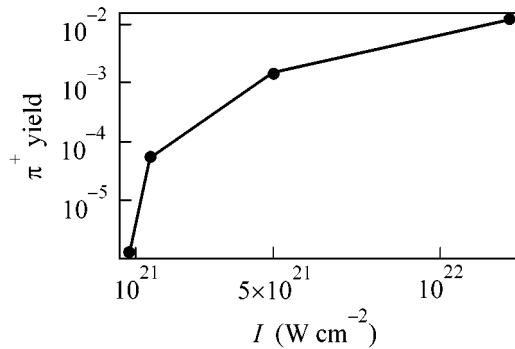**Fig. 2.** The number of forward accelerated protons with energy exceeding 140 MeV vs. laser intensity.

Fig. 3. Pion yield (per a proton) as a function of pulse intensity. The curve corresponds to the π^+ production in the proton collisions with the C nuclei.

stance behind the foil. The number N_p of accelerated protons with energy higher than 140 MeV is shown in Fig. 2 as a function of laser intensity. The accelerated protons will react with the nuclei of the substance in a layer of thickness on the order of proton stopping range, which is mainly determined by the ionization loss. The number of produced pions is lesser than the number of accelerated protons in a ratio equal to the ratio of proton stopping range to the proton path associated with π^+-production reaction. Quantitatively, this number,

$$N_\pi = \frac{1}{M_a} \int\limits_0^\infty d\epsilon \frac{dN}{d\epsilon} \int\limits_0^\epsilon d\epsilon' \frac{\sigma(\epsilon')}{W(\epsilon')}, \qquad (2)$$

is determined by the cross section σ for reaction $p + A \longrightarrow \pi^+ \dots$, where A is a nucleus with mass M_a, the stopping loss W (MeV cm^2/g) of protons in the substance a, and the pion number distribution in energy $dN/d\epsilon$.

We considered carbon and germanium targets as examples of light and heavy nuclear targets, respectively. Pion yield (2) per one proton is presented for the

carbon nuclei in Fig. 3, where the data for σ and W are taken from [17]. Despite the fact that the reaction cross section for pion production far above the threshold behaves as $A^{2/3}$ (A is the nucleus atomic number), the overlap integral in Eq. (2) shows little dependence on the atomic number. Our calculations showed that the pion yield in germanium differs from its value in carbon by only 9–15%.

Our calculations can be used to predict the laser-intensity threshold for pion production. This threshold is clearly seen in Fig. 3 at $I_{th} \sim 10^{21}$ W/cm^2. At $I = 5 \times 10^{21}$ W/cm^2, the pion production yield is 10^{-3}. For 4×10^{11} accelerated protons, this provides a value of 4×10^8 particles per shot for the total π^+ yield, which is five orders of magnitude higher than the photopion yield obtained under similar conditions in [10]. Pions can be most simply identified by the standard method from the $\pi\mu$ decay, because the lifetime of π^+ is short, $\tau_\pi \simeq 26$ ns. At a pulse repetition rate of 1 kHz, the laser muon production will offer advantages over the conventional accelerator methods and provide a muon flux of 10^{14}–10^{15} s^{-1}.

At first glance, the value of $\sim 10^{21}$ W/cm^2 found above for the pion production threshold can be attained using low-energy lasers, provided that the pulse duration equals several femtoseconds. This is quite possible in current laser techniques. However, there is a fundamental limitation that requires a considerably longer pulse duration. The reason is that, due to a large mass M of ions (protons), they are accelerated in a certain finite time τ_i, which is determined by the condition $\tau_i \sim d/v$, where v is the ion velocity, $v \sim \sqrt{T_h/M}$, and d is the length of accelerating interval $d \sim \lambda_D$, where $\lambda_D \sim (T_h/e^2 n_h)^{1/2}$ is the Debye radius of hot electrons with density n_h; i.e., $\tau_i \sim \sqrt{M/e^2 n_h}$. Taking a value on the order of critical density in estimating the density n_h of hot electrons, one obtains $\tau_i \sim 100$ fs. Since the charge-separation field is sustained by the laser, its duration must exceed τ_i, in order that the protons have time to accelerate to the maximal energy determined by the charge-separation field. On the other hand, the smallest attainable focal spot size is equal to several microns for high-power lasers. Hence, it follows that, to produce pions, the laser output should be as high as several tens of joules.

In the above examples of pion production in the proton collisions with nuclei, the pion distribution is virtually isotropic. At the same time, for the hydrogen-containing nuclear targets, where pions may be produced in the p–p collisions, one can expect the generation of directed pion and neutrino fluxes, provided that the proton energy far exceeds 1 GeV, i.e., at $I > 10^{23}$ W/cm^2 according to the scaling law discussed above. The lifetime of pions with energies up to several GeV is considerably larger than τ_π. This opens the way to their subse-

quent acceleration by the laser plasma method of particle acceleration in a underdense plasma [18] to produce ultrahigh-energy pions, which are, as yet, present only in cosmic rays. However, contrary to the latter, the laser generation of ultrahigh-energy pions is predictable.

In summary, numerical modeling of the interaction of a short relativistically strong laser pulse with plasma produced by the irradiation of a foil has been carried out in this work to investigate the generation of protons with energies of hundreds of MeV and pion production in proton collisions with light and heavy nuclei. The laser intensity threshold is determined at which pion production should be expected, and the pion yield is obtained as a function of laser intensity. This effect corresponds to the nuclear regime of interaction between the radiation of a high-power laser and a substance. The mastering of this effect will allow the development of a new exploratory base for high-energy physics.

REFERENCES

1. V. Yu. Bychenkov, V. T. Tikhonchuk, and S. V. Tolokonnikov, Zh. Éksp. Teor. Fiz. **115**, 2080 (1999) [JETP **88**, 1137 (1999)].

2. S. V. Bulanov, T. Zh. Esirkerov, F. Califano, *et al.*, Pis'ma Zh. Éksp. Teor. Fiz. **71**, 593 (2000) [JETP Lett. **71**, 407 (2000)].

3. A. Maksimchuk, S. Cu, K. Flippo, *et al.*, Phys. Rev. Lett. **84**, 4108 (2000).

4. E. L. Clark, K. Krushelnick, M. Zepf, *et al.*, Phys. Rev. Lett. **85**, 1654 (2000).

5. S. P. Hatchett, C. G. Brown, Th. E. Cowan, *et al.*, Phys. Plasmas **7**, 2076 (2000); R. A. Snavely, M. H. Key, S. P. Hatchett, *et al.*, Phys. Rev. Lett. **85**, 2945 (2000).

6. K. Krushelnick, E. L. Clark, M. Zepf, *et al.*, Phys. Plasmas **7**, 2055 (2000); E. L. Clark, K. Krushelnick, J. R. Davies, *et al.*, Phys. Rev. Lett. **84**, 670 (2000).

7. K. Nemoto, A. Maksimchuk, S. Banerjee, *et al.*, Appl. Phys. Lett. **78**, 595 (2001).

8. S. C. Wilks, A. B. Langdon, T. E. Cowan, *et al.*, Phys. Plasmas **8**, 542 (2001).

9. A. Pukhov, Phys. Rev. Lett. **86**, 3562 (2001).

10. S. Karsch, D. Habs, T. Schatz, *et al.*, Laser Part. Beams **17**, 565 (1999).

11. A. V. Kuznetsov, T. Zh. Esirkepov, F. F. Kamenets, and S. V. Bulanov, Fiz. Plazmy **27**, 225 (2001) [Plasma Phys. Rep. **27**, 211 (2001)].

12. K. B. Wharton, S. P. Hatchett, S. C. Wilks, *et al.*, Phys. Rev. Lett. **81**, 822 (1998).

13. V. A. Buts and A. V. Buts, Zh. Éksp. Teor. Fiz. **110**, 818 (1996) [JETP **83**, 449 (1996)].

14. S. C. Wilks, W. L. Kruer, M. Tabak, and A. B. Langdon, Phys. Rev. Lett. **69**, 1383 (1992).

15. G. S. Sarkisov, V. Yu. Bychenkov, V. N. Novikov, *et al.*, Phys. Rev. E **59**, 7042 (1999).

16. Y. Sentoku, T. V. Liseikina, T. Zh. Esirkepov, *et al.*, Phys. Rev. E **62**, 7271 (2000).

17. B. Jakobsson, Yu. Murin, and V. G. Khlopin, Nucl. Phys. A **630**, 184 (1998); http://www.triumf.ca/triumf-handbooks; http://physics.nist.gov/Star.

18. T. Tajima and J. M. Dawson, Phys. Rev. Lett. **43**, 267 (1979).

Translated by V. Sakun

Spin Correlations in Ni–Mn–Ga

V. V. Runov[1,*], Yu. P. Chernenkov[1], M. K. Runova[1], V. G. Gavriljuk[2], and N. I. Glavatska[2]

[1]*Petersburg Nuclear Physics Institute, Russian Academy of Sciences, Gatchina, Leningrad region, 188350 Russia*
*runov@mail.pnpi.spb.ru
[2]*Institute of Metal Physics, National Academy of Sciences of Ukraine, Kiev, 252680 Ukraine*
Received November 8, 2001; in final form, November 20, 2001

Results of measuring small-angle neutron scattering and neutron depolarization in a $Ni_{49.1}Mn_{29.4}Ga_{21.5}$ single crystal in the temperature range $15 < T < 400$ K and in the range of magnetic fields $0 < H < 4.5$ kOe are presented. The characteristic temperatures of the alloy were found to be as follows: $T_C = 373.7$ K and the martensite transition temperature $T_m = 301$–310 K. The magnetic critical scattering at T_C and the scattering at $T < T_C$ were adequately described by the relationship $I_m = A(q^2 + \kappa^2)^{-2}$ (q is the transferred wave vector and $R_c = 1/\kappa$ is the correlation radius), and the temperature dependences of the A and R_c scattering parameters were determined. Left–right asymmetry was observed at $150 < T < T_m$ in the scattering of neutrons polarized along or opposite to the applied field. This asymmetry was due to the inelastic magnetic interaction of neutrons in the sample. The magnetization of the alloy at T_m, critical scattering at $T \simeq T_C$, anomalies in scattering, and the softening of magnetic excitations at $150 < T < T_m$ are discussed. © 2001 MAIK "Nauka/Interperiodica".

PACS numbers: 75.25.+z; 72.15.Qm; 61.12.Ex; 81.30.Kf

The ternary intermetallic Ni_2MnGa Heusler alloy undergoes a martensite transition from the cubic phase of the $L2_1$ type to the tetragonal phase with the axis ratio $c/a = 0.94$ [1]. The uniqueness of this alloy is in the fact that martensite transformations occur in the ferromagnetic state; therefore, it is one of the materials in which the magnetic shape memory effect (MSME), magnetoelastic properties, and the domain structure of the ferromagnetic phase are widely investigated [1–7]. Characteristic temperatures and the structure of the martensite phase are extremely sensitive to the deviation of the alloy composition from the stoichiometric one; for example, the martensite transition temperature may vary over several hundreds of degrees [4–8], which is promising for possible technical applications. Apart from MSME and the complex structure in the martensite phase, a number of other interesting physical phenomena are observed in the alloy, such as a softening of the phonon mode [9–11] and a change in the spin density distribution at the martensite transition [12].

This work is devoted to measuring small-angle polarized-neutron scattering (SAPNS) by a nonstoichiometric Ni–Mn–Ga sample with the aim of studying mesoscale magnetic nonuniformities over a wide range of temperatures and magnetic fields. Mesoscale defects in these materials are considered along with the atomic structure to explain premartensitic phenomena observed in the system (see, for example, [13, 14]). As to spin correlations and spin dynamics, these phenomena, of course, are interrelated with the atomic struc-

ture; however, as far as we know, this question has not been investigated in the literature.

1. Samples and experimental procedures. Single-crystal samples of the nonstoichiometric $Ni_{49.1}Mn_{29.4}Ga_{21.5}$ alloy were investigated. According to [7], the composition has the following characteristic temperatures as determined by measuring its magnetic susceptibility: the Curie temperature $T_C \approx 375$ K and the martensite transition temperature is in the range $T_m \approx 302$–314 K. It was shown in the same work that a reversible 5.3% MSME is accomplished in samples of this composition after a certain magnetic and mechanical treatment.

Experiments were carried out on a VEKTOR small-angle polarized-neutron scattering setup [15] (WWR-M reactor, Gatchina) at the wavelength $\lambda = 9.2$ Å ($\Delta\lambda/\lambda = 0.25$). A setup equipped with a 20-counter (^3He) detector and a multichannel analyzer works in the slit geometry in the range of scattering vectors $0 < q < 3 \times 10^{-1}$ Å^{-1} (**q** = **k** – **k**', where **k** and **k**' are the wave vectors of the incident and scattered neutrons, respectively). The neutron beam polarization was determined as $P = (I^+ - I^-)/(I^+ - I^-)$, where $I^{\pm}$ is the intensity of neutrons with the corresponding spin state with respect to the magnetic field. The initial polarization of the neutron beam incident on the sample was $P_0 \cong 0.94$. The samples for SAPNS measurements were shaped as rectangular plates, 10×30 mm in size with the thickness $L = 1$ and 2 mm, cut from a single-crystal ingot so that the faces of the samples coincided with {100} planes with an accuracy of several degrees. Neutron

diffraction measurements confirmed the occurrence of a structural transition from the cubic to tetragonal phase in the temperature range 301–315 K ($a = 6.018$, $c = 5.67$ Å, $c/a = 0.94$).

Experiments in a magnetic field were carried out in the "inclined" geometry, when a sample is magnetized at an angle φ to the direction of the incident neutron beam. It was shown in [16, 17] that the left–right asymmetry of scattering in the scattering plane can be observed in this geometry for neutrons initially polarized along and opposite to the direction of the applied magnetic field. This asymmetry is due to the inelastic magnetic interaction of neutrons in the sample. In this experiment, the magnetic field in the horizontal plane was applied along the face 10 mm in width, that is, **H** ∥ [100], at the angle $\varphi \simeq 55°$ to the direction of the incident neutron beam. The measurements were performed in magnetic fields $0 < H < 4500$ Oe. The low-temperature measurements in the temperature range $15 \le T \le 320$ K were carried out in an RNK10-300 cryorefrigerator, and the high-temperature measurements were performed in a vacuum furnace. The long-term temperature stabilization of the samples was better than $\simeq 0.1$ K.

2. Results of measurements. Variations of the polarization of neutrons, passed through a sample in various fields, with temperature are presented in Fig. 1. A sample preheated up to $T > T_C$ was mounted in the cryorefrigerator and was placed in a magnetic field at room temperature ($T_R \simeq 295$ K) in the inclined geometry mentioned above. It is evident in Fig. 1a, curve *1*, that the polarization of the transmitted neutrons at T_R detected by the central detector $P \sim 0$; that is, the sample is not magnetized uniformly in this field but consists of magnetic domains magnetized in different directions. It should be noted that a weak rearrangement of the magnetic structure proceeds in the field even at T_R. For example, a sample 1-mm thick, which is easier magnetized in a field of 4.2 kOe, exhibited a linear rise in polarization at T_R from 13 to 15% for 5 h. Variations of the same scale were also exhibited in the intensity of the scattered neutrons. A sharp increase in the uniform magnetization of the sample accompanied with a rise in polarization up to $P \sim 90\%$ was observed at T_m, Fig. 1a, curve *1*. Upon further cooling the sample in the field down to T_R, a temperature hysteresis was observed. In this case, the polarization of neutrons did not drop to zero but only decreased down to $\sim 60\%$. Moreover, upon switching the magnetic field off at T_R followed by switching it on, the sample was uniformly magnetized after several days up to the level $P \sim 60\%$ in a field of 4.2 Oe, and the heating–cooling cycle in the vicinity of the structural transition ran along curve *2* in Fig. 1a. Typical heating–cooling cycles for samples differing in thickness in fields of 4.2 and 1 kOe are shown in Fig. 1a, curve *3*, and Fig. 1b in the range $T = 18–300$ K.

As was mentioned above, a slow rearrangement of the magnetic mesostructure in a field proceeds even at T_R; however, the rate of variations sharply increases at
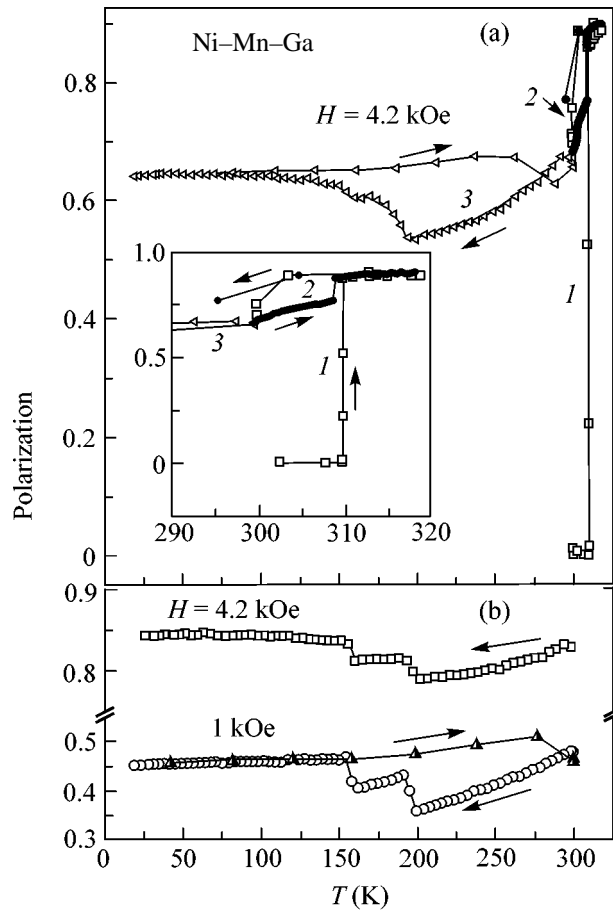

Fig. 1. Temperature dependence of the polarization of neutrons detected by the central detector normalized to P_0: (a) a sample with the thickness $L = 2$ mm (*1* (□), the first heating–cooling cycle in the vicinity of T_m after overheating the sample above T_C; *2* (●), one of the repeated heating–cooling cycles in the vicinity of T_m; *3* (△), a cooling–heating cycle in the temperature range 300–18 K); (b) a sample with $L = 1$ mm in various fields.

a temperature close to T_m. The phase transition kinetics in a field observed both by the variation of the polarization and by the variation of the scattering intensity in the vicinity of T_m is shown in Fig. 2. This figure demonstrates that the transition under these conditions is completed in ~ 30 min. Even though $P(t)$ in this case attains saturation at the given temperature, it does not reach its maximum value in the measurement time, as distinct from $P(T > T_m)$ in the same field, Fig. 1, curve *1*. The difference comprises $\sim 2\%$.

The temperature dependence of the small-angle neutron scattering intensity ($I = I^+ + I^-$) in various magnetic fields for one of the scattering vectors is shown in Fig. 3. Note the occurrence of two temperature ranges in which strong variations of the scattering intensity are observed in fields $H < 4$ kOe: (1) the range $T_m < T < T_C$, in which the scattering intensity virtually linearly grows at $T < T_C$ and sharply drops at the martensite
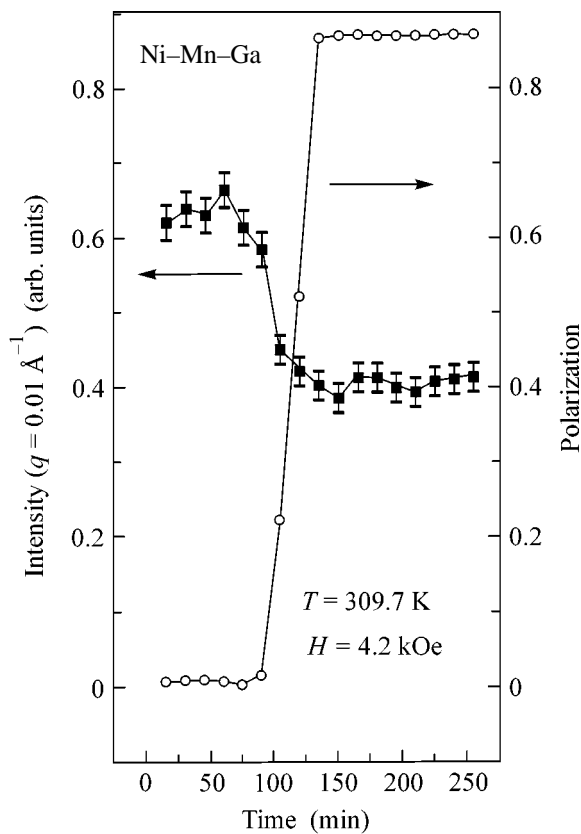
Fig. 2. Time dependence of the intensity of small-angle scattering and the polarization normalized to P_0 on magnetization of a sample with $L = 2$ mm in the vicinity of T_m.

Fig. 3. Temperature dependence of (*1–4*) the intensity of small-angle neutron scattering for a sample with $L = 2$ mm with the transferred momentum $q \simeq 0.01$ Å^{-1} and (*5*) the polarization: (*1*) $H \simeq 0$, ($\lesssim 2$ Oe); (*2*) $H = 10$ Oe; (*3*) $H = 1$ kOe; (*4*) $H = 4.2$ kOe. In measurements of *1* and *5*, the sample was preheated above T_C in $H \simeq 0$; measurements of *2–4* were carried out after heating above T_m in a field of ≈ 4.2 kOe; $T_C = 373.7$ K; $T_m = 301–310$ K.

transition temperature, Fig. 3, curve *1*; and (2) the range $100 < T < 250$ K, in which rather strong variations of scattering and polarization with a temperature hysteresis occur, Figs. 1 and 3, curves *1–4*. A small variation of polarization in the vicinity of T_m is also observed in the field $H \lesssim 2$ Oe, in which measurements were carried out, Fig. 3, curve *5*. The scattering intensities in weak fields, Fig. 3, curves *1* and *2*, rather strongly differ; however, this difference is most likely associated with the magnetic prehistory of the sample. Curve *1* corresponds to measurements carried out in the magnetic field $H \lesssim 2$Oe with the sample preheated up to $T > T_C$, whereas curve *2* corresponds to measurements in the field $H \simeq 10$ Oe after magnetizing the sample in the field $H = 4.2$ kOe by the procedure described above.

Figure 4 presents a characteristic temperature dependence (statistically significant for $q = k\Theta \lesssim 0.015$ Å^{-1}, where Θ is the scattering angle in the horizontal plane) of the difference in the scattering of neutrons $\Delta(T) = I^+ - I^-$ polarized along and opposite to the applied field $H = 4.2$ kOe for counters symmetrical with respect to $q = 0$. The pulse dependence $\Delta(q)$ at $T \simeq 200$ K is given in the same figure (see inset). It is evident in Fig. 4 that the neutron scattering in the temperature range 300–150 K depends on the direction of the
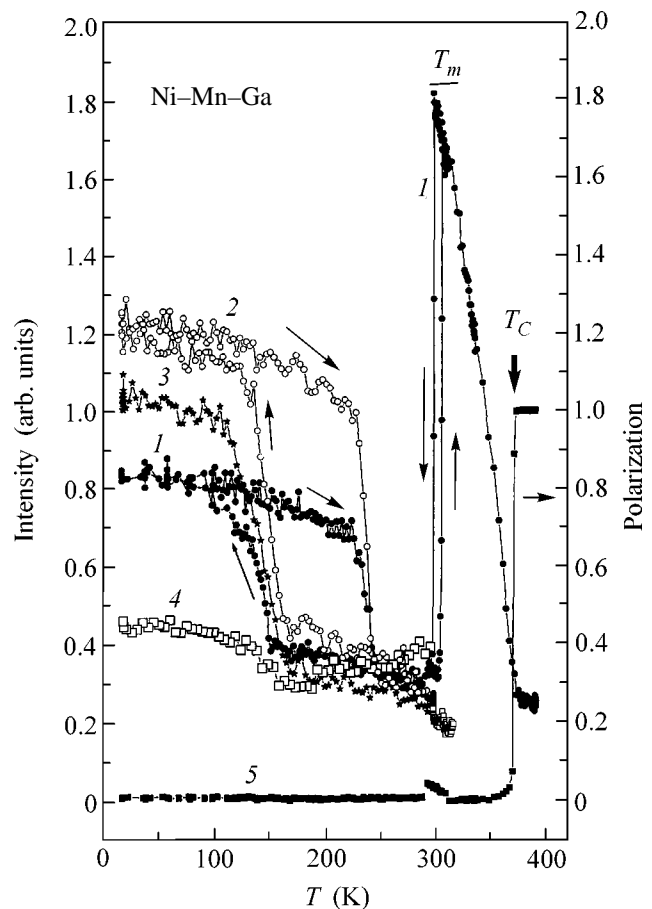
initial neutron polarization ($\Delta \neq 0$, $\Delta/I \lesssim 20\%$), and well-defined left–right asymmetry is observed.

3. Analysis of measurements and discussion. Let us first discuss the process of magnetization of samples monitored by the variation of the polarization and small-angle scattering of neutrons. It is known that (see, for example, [18–20]) the change in polarization detected by the central counter is determined by the integral magnetic neutron scattering Σ by large-scale magnetic fluctuations with the characteristic size $R > 1/q_{min}$ (q_{min} is the counter resolution)

$$P = P_0 \exp(-g\Sigma L), \qquad (1)$$

where $g < 2$ is the coefficient depending on the polarization orientation of neutrons incident on the sample with respect to **k**. Hence, the variations of polarization in Figs. 1–3 basically characterize the rearrangement of the large-scale magnetic structure ($q_{min} \gtrsim 10^{-3}$ Å^{-1}),

whereas the variations of small-angle scattering characterize the evolution of magnetic nonuniformities of scale $R < 1/q_{min}$.

Changes in the magnetization of Ni–Mn–Ga alloys in the vicinity of T_m were observed in all the studies in which magnetic measurements were performed. We note some features observed in this work on measuring the neutron polarization. Firstly, the $P(T, H)$ dependence in Fig. 1 can be explained by the fact that the magnetic structure formed in the process of transition to the high-symmetry cubic phase upon heating in a field is also predominantly retained on cooling, that is, on returning to the low-symmetry tetragonal phase. Evidently, the sample undergoes peculiar magnetic texturing, which is one of the methods for magnetic treatment of the given alloy. Secondly, a temperature hysteresis occurs in the variation of the magnetic mesostructure in the range $150 < T < 300$ K, that is, in the martensite phase. It is apparent in Figs. 1, 3, and 4 that abrupt changes in depolarization and changes in scattering intensity are observed both in a magnetic field and at $H \simeq 0$. Changes are also observed in the magnetic dynamics in the sample, which will be discussed below. It may be suggested that a structural rearrangement proceeds in the sample at these temperatures. Finally, relaxation changes in the magnetic mesostructure occur at $T < T_m$ in a magnetic field, which terminate in an avalanche-type transition to the cubic phase at $T \lesssim T_m$ (Fig. 2). Considering the long-term relaxation observed experimentally and the wide range of magnetic nonuniformities, one may expect that relaxation processes occur in the given material analogous to those observed in spin glasses.

Let us start the discussion of small-angle scattering from the critical scattering in the vicinity of T_C (Fig. 3). The first questions that should be solved in studying critical scattering are the determination of the phase transition temperature T_C and the determination of the $R_c(\tau)$ dependence ($\tau = T/T_C - 1$). It was shown theoretically in [18] and experimentally in studying critical scattering in Fe [21] that, in the case of a second-kind phase transition, T_C in the $P(T)$ dependence of polarization must be located at a level of thermal-neutron depolarization. This level does not exceed several percent for classical ferromagnets because of the smallness of the depolarization, due to the neutron scattering by critical magnetic fluctuations. Its intensity $I_m(q, T)$ is described by the Ornstein–Zernicke (O–Z) equation $I_m \propto [q^2 + \kappa^2]^{-1}$ (where $\kappa = 1/R_c$), under the assumption that $R_c \longrightarrow \infty$ at $T = T_C$. The subsequent and main depolarization at $T < T_C$ proceeds on magnetic domains. Therefore, SAPNS experiments primarily provide information on a narrow region of temperatures $T_{beg} \lesssim T_C$, where T_{beg} is the beginning temperature of depolarization. The subsequent refinement of T_C and the $R_c(\tau)$ dependence can be obtained from an analysis of small-angle scattering using the O–Z equation. It was found
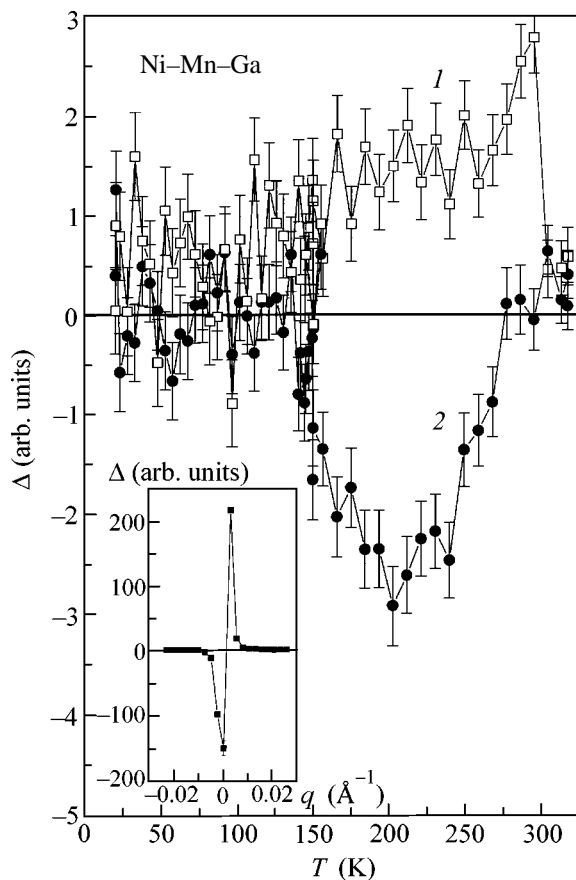

Fig. 4. Temperature and pulse (inset) dependences of the difference of neutron scattering $\Delta = I^+ - I^-$ by a sample with $L = 2$ mm in a field of 4.2 kOe: (*1*) $q = k\Theta \simeq 0.01$ Å^{-1}; (*2*) $q = k\Theta \simeq -0.01$ Å^{-1}. The curve in the inset was obtained at $T = 200$ K.

that the intensity of magnetic small-angle scattering $I_m(q, T) = I(q, T) - I(q, \sim395$ K$)$ at $T \gtrsim T_{beg} \simeq 373.7$ K (at a level of depolarization $\leqslant 0.5\%$) is described in this work not by the O–Z equation but by the equation

$$I_m(q) = A/(q^2 + \kappa^2)^2, \qquad (2)$$

where A is a parameter. The results of fitting the small-angle scattering by Eq. (2), with allowance made for the resolution function of the instrument, are shown in Fig. 5c. It is known that Eq. (2) describes scattering with the spin correlator $\langle S_i S_j \rangle \propto \exp(-r/R_c)$, which decreases with increasing distance r much less sharply than that for the O–Z function. The fact that the critical scattering described by the O–Z equation is not observed in the given system means that either this scattering is small and requires a setup with a larger efficiency for its detection or the phase transition is not, strictly speaking, a second-kind transition. The question still remains open. We assume that the transition temperature in the given system $T_C \simeq T_{beg}$, because
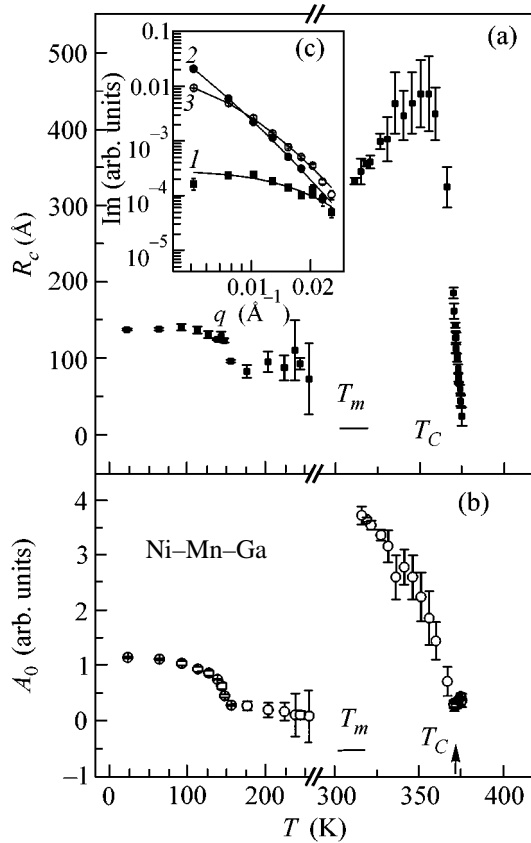
Fig. 5. (a) and (b) Temperature dependence of the fitting parameters for the intensity of neutron scattering by a sample with $L = 2$ mm at $H \approx 0$ by Eq. (2) and (c) pulse dependence of scattering I_m at (*1*) 373.9 K; (*2*) 359 K; and (*3*) 92.6 K; solid lines in the inset correspond to the calculation by Eq. (2); $T_C = 373.7$ K; $T_m = 301$–310 K.

there is simply no other distinguished temperature in this region.

The parameters obtained by fitting the scattering intensity using Eq. (2) are shown in Fig. 5. Equation (2) also adequately describes small-angle scattering below T_C in the entire region of measured temperatures (see Fig. 5c), except for the range of the martensite transition itself. The small-angle scattering observed at $T < T_C$ can be caused by both nuclear and magnetic nonuniformities. However, considering that it depends essentially on the magnetic field (see Fig. 3), there is reason to believe that the magnetic scattering is the determining factor. The reason for the magnetic scattering in this region can be both the domain structure of the sample in the austenite phase and nucleation centers of the new martensite phase of scale $\sim R_c$. These formations of the new phase differ from the cubic phase in the moment and spin density distribution [12] and must contribute to the intensity of magnetic small-angle scattering. It is evident in Fig. 5 that both R_c and the parameter $A_0 = AR_c$, which is proportional to the amplitude of scatter-

ing by magnetic nonuniformities and to their concentration, grow virtually linearly with decreasing temperature in the range $T_m < T < T_C$ at $H \approx 0$. A sharp breakdown of the growth of these parameters comes at $T \cong T_m$. Assuming that the intensity of scattering by the regions with the martensite phase is the determining factor, one may infer that a percolation-type phase transition is evidently observed at T_m. In this case, the system at $T \simeq T_m$ is homogenized on the magnetic mesoscale to such a degree that the magnetization in the guiding field $H \lesssim 2$ Oe becomes evident: the polarization in this temperature region differs markedly from zero, see Fig. 3, curve *5*. On further cooling, a less pronounced rise in the parameters is observed at $T \sim 150$ K.

The spin-wave stiffness D can be calculated from measurements of the left–right asymmetry of polarized-neutron scattering (see Fig. 4) by measuring the cutoff angle Θ_0 such that the intensity of the asymmetric part sharply decreases when it is exceeded [16, 17]. It is known that, in the spin-wave approximation, i.e., under the assumption that the energy of spin waves $\omega = Dq^2$, the spin-wave stiffness is related to Θ_0 by the equation $D = E/\Theta_0 k^2$, where E is the energy of neutrons. Because the angular resolution of the instrument was insufficient, it was not possible to determine Θ_0 to a sufficient accuracy in the given experiment; therefore, the spin-wave stiffness can only be estimated in the range $150 < T < T_m$ at a level of $D \lesssim 140$ meV Å^2. It may be suggested that the spin-wave stiffness significantly exceeds this value outside this temperature range in the ferromagnetic region; therefore, $\Theta_0 \lesssim (\lambda/2\pi)q_{\min}$, and the left–right asymmetry of scattering is not observed at the available resolution of the instrument. Apparently, a softening of the magnetic mode occurs in the sample in the range $150 < T < T_m$. Apart from the asymmetric part, the part symmetrical with respect to $q = k\Theta$ was observed in the experimental dependence $\Delta(T) = I^+ - I^-$ in the same temperature range. This part reaches a maximum at $q \simeq 0$. This means (see, for example, [16, 17, 20, 22]) that magnetic–nuclear interference on mesoscale nonuniformities occurs in neutron scattering at $150 < T < T_m$. As a whole, there is reason to suggest that structural changes, which are accompanied by changes in the magnetic mesostructure and in spin dynamics, proceed in the sample in this temperature range.

The measurements of small-angle polarized-neutron scattering performed on $Ni_{49.1}Mn_{29.4}Ga_{21.5}$ samples demonstrated the informativeness of the method. Temperature dependences of scattering parameters were obtained. Changes in the magnetic mesostructure and a softening of the spin dynamics in the martensite phase were found at $150 < T < T_m$. These effects evidently originate from structural changes. The critical scattering at T_C was measured, which has not been interpreted so far. The experiment showed the necessity of subsequent neutron investigations of both the structure and

spin dynamics in these alloys, which are commonly classified as "smart materials."

REFERENCES

1. P. J. Webster, K. R. Ziebeck, and S. L. Town, Philos. Mag. B **49**, 295 (1984).

2. A. N. Vasil'ev, V. V. Kokorin, Yu. I. Savchenko, and V. A. Chernenko, Zh. Éksp. Teor. Fiz. **98**, 1437 (1990) [Sov. Phys. JETP **71**, 803 (1990)]; Zh. Éksp. Teor. Fiz. **109**, 973 (1996) [JETP **82**, 524 (1996)].

3. K. Ullakko, J. Huang, C. Kantner, *et al.*, Appl. Phys. Lett. **69**, 1966 (1996).

4. S. L. Murray, M. Farinelli, C. Kantner, *et al.*, J. Appl. Phys. **83**, 7297 (1998).

5. R. D. James and M. Wuttig, Philos. Mag. A **77**, 1273 (1998).

6. R. C. O'Handley, J. Appl. Phys. **83**, 3263 (1998).

7. O. Heczko, N. Glavatska, V. Gavriljuk, and K. Ullakko, in *Proceedings of the 8th European Magnetic Materials and Applications Conference, Kiev, 2000* (Trans. Tech. Publ., Switzerland, 2000), p. 341.

8. A. N. Vasil'ev, A. D. Bozhko, V. V. Khovailo, *et al.*, Phys. Rev. B **59**, 1113 (1999).

9. G. Fritsch, V. V. Kokorin, and A. Kempf, J. Phys.: Condens. Matter **6**, L107 (1994).

10. A. Zheludev, S. M. Shapiro, P. Wochner, *et al.*, Phys. Rev. B **51**, 11310 (1995).

11. U. Stuhr, P. Vorderwisch, V. V. Kokorin, *et al.*, Phys. Rev. B **56**, 14360 (1997).

12. P. J. Brown, A. Y. Bargawi, J. Crangle, *et al.*, J. Phys.: Condens. Matter **11**, 4715 (1999).

13. J. A. Krumhansel and R. J. Gooding, Phys. Rev. B **39**, 3047 (1989).

14. W. Cao, J. A. Krumhansl, and R. J. Gooding, Phys. Rev. B **41**, 11319 (1990).

15. S. V. Grigor'ev, O. A. Gubin, G. P. Kopitsa, *et al.*, Preprint PIYaF-2028 (Gatchina, 1995).

16. A. I. Okorokov, A. G. Gukasov, V. V. Runov, *et al.*, Zh. Éksp. Teor. Fiz. **81**, 1462 (1981) [Sov. Phys. JETP **54**, 775 (1981)].

17. A. V. Lazuta, S. V. Maleev, and B. P. Toperverg, Zh. Éksp. Teor. Fiz. **81**, 1475 (1981) [Sov. Phys. JETP **54**, 782 (1981)].

18. S. V. Maleev and V. A. Ruban, Zh. Éksp. Teor. Fiz. **62**, 415 (1972) [Sov. Phys. JETP **35**, 222 (1972)].

19. S. V. Grigor'ev, S. A. Klimko, S. V. Maleev, *et al.*, Zh. Éksp. Teor. Fiz. **112**, 2134 (1997) [JETP **85**, 1168 (1997)].

20. V. V. Runov, D. Yu. Chernyshov, A. I. Kurbakov, *et al.*, Zh. Éksp. Teor. Fiz. **118**, 1174 (2000) [JETP **91**, 1017 (2000)].

21. A. I. Okorokov, V. V. Runov, A. G. Gukasov, and G. M. Drabkin, Izv. Akad. Nauk SSSR, Ser. Fiz. **42**, 1770 (1978).

22. V. V. Runov, H. Glattli, G. P. Kopitsa, *et al.*, Pis'ma Zh. Éksp. Teor. Fiz. **69**, 323 (1999) [JETP Lett. **69**, 353 (1999)].

Translated by A. Bagatur'yants

The Berezinskii–Kosterlitz–Thouless Transition and Correlations in the *XY* Kagomé Antiferromagnet[1]

V. B. Cherepanov[1], I. V. Kolokolov[2], and E. V. Podivilov[3]

[1] Hummingberg Ltd., Toronto, Ontario, Canada MZH 2S6
[2] Budker Institute of Nuclear Physics, Novosibirsk, 630090 Russia
[3] Institute of Automation and Electrometry, Russian Academy of Sciences, Novosibirsk, 630090 Russia

Received November 20, 2001

The problem of the Berezinskii–Kosterlitz–Thouless transition in the highly frustrated *XY* kagomé antiferromagnet is solved. The transition temperature is found. It is shown that the spin correlation function exponentially decays with distance even in the low-temperature phase, in contrast to the order parameter correlation function, which decays algebraically with distance. © *2001 MAIK "Nauka/Interperiodica".*

PACS numbers: 75.10.Hk; 75.50.Ee

Generally, *XY* spins on two-dimensional lattices undergo a Berezinskii–Kosterlitz–Thouless (BKT) transition [1, 2]. If there is no frustration, the physics of this transition does not depend on the specifics of the lattice structure. At finite temperatures, the behavior of a system is governed by spin waves and vortices. They are well defined in continuum limit of the theory. In the low-temperature phase, the spin vortices are bound in pairs with zero topological charge, and spin correlators decay with distance algebraically. One can also define the vorticity field demonstrating nontrivial dynamical correlations [3]. In the BKT transition point, the vortex–antivortex interaction becomes screened, pairs disintegrate, and the spin correlation length becomes finite. By contrast, the *XY* antiferromagnet on the two-dimensional kagomé lattice (see figure) has infinitely many ground states, and its description in terms of continuous field theory is not justified.

In this paper, we compute the BKT transition temperature in such systems. In [4], it was suggested that the true order parameter here is $\eta = e^{3i\theta}$, where θ is the angle of a spin. It is invariant with respect to any arbitrary choice of ground states, which are a subset of local $2\pi/3$ spin rotations. Therefore, this order parameter can change smoothly in the plane. The phase transition consists in the emergence of a finite correlation length of the variable η. Indirect evidence of this was obtained by Monte-Carlo simulations in [5, 6]. As for the correlation length of spins itself, we show here that it is finite starting at an arbitrary low temperature. This is the inevitable consequence of finite values of energy barriers separating different vacua.

In order to take into account the special structure of the kagomé lattice, we start with the approach developed in [7] (see also [8]). The kagomé lattice consists

of triangles and hexagons (figure). The Hamiltonian of the kagomé antiferromagnet can be represented as a sum of squares of the total spins $\mathbf{S}_t$ in triangles $\{t\}$ of the nearest neighbors:

$$H = \frac{\kappa}{2}\sum_t (\mathbf{S}_t)^2. \tag{1}$$

Each spin participates in two triangles. The ground-state energy is equal to zero, and there are infinitely many ground states with $\mathbf{S}_t = 0$. In any ground state, the angles between neighboring spins are equal to $\pm 2\pi/3$.

The partition function of the *XY* kagomé antiferromagnet can be represented as an integral of a function defined on the lattice bonds:

$$Z(\beta) = \int \exp\left(-\beta \sum_{\mathbf{r}, \mathbf{a}} \cos \Theta_{\mathbf{r}, \mathbf{a}}\right) \prod_{\mathbf{r}} d\theta(\mathbf{r}), \tag{2}$$

$$\Theta_{\mathbf{r}, \mathbf{a}} \equiv \theta(\mathbf{r} + \mathbf{a}) - \theta(\mathbf{r}),$$

where $\mathbf{r}$ denotes positions on the kagomé lattice, $\mathbf{a}$ are three lattice vectors directed along the antiferromag-
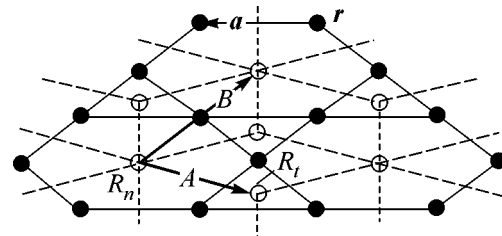
The kagomé lattice (filled dots) with antiferromagnetic bonds (continuous lines), and the dual lattice (circles) and its bonds (dashed lines).

---

[1] This work was submitted by the authors in English.

netic bonds between nearest neighbors, $\theta_{\mathbf{r}}$ are the spin angles, and $\beta = \kappa S^2/2T$ is the dimensionless inverse temperature.

The 2π periodicity of the angular variables allows one to expand the statistical weight in Eq. (2) in Fourier series with the coefficients $I_{n(\mathbf{r}, \mathbf{a})}(-\beta)$:

$$\exp\left(-\beta \sum_{\mathbf{r}, \mathbf{a}} \cos\Theta_{\mathbf{r}, \mathbf{a}}\right)$$
$$= \prod_{(\mathbf{r}, \mathbf{a})} \sum_{n(\mathbf{r}, \mathbf{a})} I_{n(\mathbf{r}, \mathbf{a})}(-\beta) \exp(in(\mathbf{r}, \mathbf{a})\Theta_{\mathbf{r}, \mathbf{a}}). \tag{3}$$

Here, $I_n(x)$ is the modified Bessel function, and integer numbers $n(\mathbf{r}, \mathbf{a})$ are located on bonds connecting nearest neighbors $\mathbf{r}$ and $\mathbf{r} + \mathbf{a}$. Then we integrate over the angles $\theta(\mathbf{r})$ and arrive at the following representation for the partition function:

$$Z(\beta) = \sum_{\{n(\mathbf{r}, \mathbf{a})\}} \prod_{\mathbf{r}} \Delta\left(\sum_{\mathbf{a}} n(\mathbf{r}, \mathbf{a})\right) \prod_{\mathbf{a}} I_{n(\mathbf{r}, \mathbf{a})}(-\beta), \tag{4}$$

where $n(\mathbf{r} + \mathbf{a}, -\mathbf{a}) = -n(\mathbf{r}, \mathbf{a})$. Here, $\{n(\mathbf{r}, \mathbf{a})\}$ denotes the set of all configurations of integers $n(\mathbf{r}, \mathbf{a})$. The Δ function ($\Delta(0) = 1$, $\Delta(n \neq 0) = 0$) expresses the conservation condition at each site of the lattice:

$$\sum_{\mathbf{a}} n(\mathbf{r}, \mathbf{a}) = 0. \tag{5}$$

As in the case of perturbation theory graphs [9], this means that the summation in Eq. (4) runs effectively over integer-valued currents $J(\mathbf{R})$ circulated in closed loops. The latter are numbered by dual lattice sites $\mathbf{R}_t$ and $\mathbf{R}_h$, which are located in centers of triangles and hexagons, correspondingly (figure). A current $n(\mathbf{r}, \mathbf{a})$ along the $\mathbf{a}$ bond is equal to the sum of currents in one triangle and in one hexagon that share the bond $(\mathbf{r}, \mathbf{a})$. This allows us to represent the partition function as follows:

$$Z(\beta) = \sum_{\{J(\mathbf{R}_h)\}} \prod_{\mathbf{R}_t} \sum_{J(\mathbf{R}_t)} \prod_{h=1}^{3} I_{J(\mathbf{R}_t + \mathbf{A}_h) + J(\mathbf{R}_t)}(-\beta). \tag{6}$$

Here, we separate sums over triangle and hexagon currents, $J(\mathbf{R}_t)$ and $J(\mathbf{R}_h)$, with centers $\mathbf{R}_t$ and $\mathbf{R}_h = \mathbf{R}_t + \mathbf{A}_h$, and h numbers of three hexagons surrounding each triangle $\mathbf{R}_t$. Further, we consider $e^{-\beta}$ as a small parameter of the theory. We will see that the inequality $e^{-\beta} \ll 1$ holds even in the BKT transition point, as it does for the square lattice [1, 2, 7]. However, the Bessel functions in Eq. (6) cannot be substituted by their asymptotic forms at $\beta \gg 1$, because the summation over $J(\mathbf{R}_t)$ results in a relatively small contribution to $Z(\beta)$. This asymptotic form corresponds to the saturation of a maximal number of nearest-neighbor bonds, which is far away from the true ground state, due to frustrations. Consequently,

the summation over the triangle currents $J(\mathbf{R}_t)$ must be performed first. To do this, we represent triple products of the Bessel functions in (6) in the integral form, which allows us to take the sum over $J(\mathbf{R}_t)$ exactly:

$$\sum_{J(\mathbf{R}_t)} \prod_{h=1}^{3} I_{J(\mathbf{R}_t + \mathbf{A}_h) + J(\mathbf{R}_t)}(-\beta) = \sum_{m = -1, 0, 1} \int\int\int_{-\pi-\pi-\pi}^{\pi\,\pi\,\pi} \frac{d\phi_1 d\phi_2 d\phi_3}{(2\pi)^3}$$
$$\times \delta(\phi_1 + \phi_2 + \phi_3 + 2\pi m)$$
$$\times \exp\left[-\sum_{h=1}^{3} i\phi_h J(\mathbf{R}_t + \mathbf{A}_h) + \beta\cos(\phi_h)\right] \tag{7}$$
$$\sim \sum_{\sigma(\mathbf{R}_t) = \pm 1} \exp\left\{\frac{i2\pi\sigma(\mathbf{R}_t)}{3}\left(\sum_{h=1}^{3} J(\mathbf{R}_h)\right)\right.$$
$$\left. -\frac{1}{6\beta}\sum_{h', h = 1}^{3} (J(\mathbf{R}_{h'}) - J(\mathbf{R}_h))^2\right\}.$$

Here, $\mathbf{R}_h = \mathbf{R}_t + \mathbf{A}_h$ for a given t. The last asymptotic relation in Eq. (7) follows from the fact that the integration over $d\phi_1 d\phi_2 d\phi_3$ at large β is saturated by the vicinity of two saddle points $\phi_h = 2\pi\sigma(\mathbf{R}_t)/3$, where $\sigma(\mathbf{R}_t) = \pm 1$ ($h = 1, 2, 3$). Thus, hexagon currents and chiralities $\sigma = \pm 1$ residing in triangles are retained. These variables include the multiple ground states. Substituting the asymptotic formula for the triple products of Bessel functions (7) into Eq. (6) and using the Poisson summation formula, we arrive at the following expression for the partition function:

$$Z(\beta) = \sum_{\{\sigma(\mathbf{R}_t)\}, \{m(\mathbf{R}_h)\}} \int \exp\left\{2\pi i \sum_{\mathbf{R}_h} J(\mathbf{R}_h) Q(\mathbf{R}_h)\right.$$
$$\left. -\frac{1}{3\beta} \sum_{\mathbf{R}_h, \mathbf{B}_h} (J(\mathbf{R}_h) - J(\mathbf{R}_h + \mathbf{B}_h))^2\right\} \prod_{\mathbf{R}_h} dJ(\mathbf{R}_h), \tag{8}$$

$$Q(\mathbf{R}_h) = m(\mathbf{R}_h) + \frac{1}{3}\sum_{\mathbf{A}_t} \sigma(\mathbf{R}_h + \mathbf{A}_t). \tag{9}$$

Here, $\mathbf{A}_t$ runs over all six triangles surrounding each hexagon, with the centers $\mathbf{R}_h$, $\mathbf{R}_t = \mathbf{R}_h + \mathbf{A}_t$ and $\mathbf{B}_h$ being the six vectors that connect the centers of nearest hexagons. Note that centers of hexagons form a triangular lattice which is dual to the hexagonal lattice.

Now, one can integrate the partition function (8) over the currents in hexagons $J(\mathbf{R}_h)$. This results in the expression for the partition function of the 2D Coulomb gas with charges $Q(\mathbf{R}_h)$ positioned at sites of the triangular lattice $\mathbf{R}_h$. Charges are 1/3-multiple; this corresponds to the $2\pi/3$-multiplicity of vortex rotations. At zero temperature, the integration over $J(\mathbf{R}_h)$ in Eq. (8)

yields conservation conditions $\prod_{\mathbf{R}_h} \delta(Q(\mathbf{R}_h))$; i.e., in any ground state, the sum of chiralities of triangles surrounding each hexagon is a multiple of 3. The problem of counting ground states is mapped onto that of coloring the hexagonal lattice [4], which was solved exactly [10]. The exact number of ground states, Z_N, is equal to $1.460099^{N/3}$, where N is the number of spins. A naive approximation assuming that chiralities of triangles surrounding each hexagon are independent and equally probable gives a good estimate of $Z_N \approx (11/8)^{N/3} = 1.375^{N/3}$ for the number of the ground states. In this estimate, we neglect correlations between chiralities of triangles surrounding neighboring hexagons. Their effect can be estimated as the inverse number of the nearest neighbors on the triangular lattice, 1/6. At finite temperatures, we divide $J(\mathbf{R})$ into slowly varying and short-wavelength fields and integrate the first over the latter. This gives the product of local statistical weights $\prod_n \exp(-3\beta\pi^2 Q_n^2/8)$, which substitutes the product of δ functions at $\beta \longrightarrow \infty$. The BKT transition point is determined by the excitations with most probable charges: $Q_n = 0, \pm 1/3$. States with the sum of chiralities of triangles surrounding a certain hexagon equal to ± 2 and ± 4 contribute to the formation of such $Q = \pm 1/3$ configurations. For a given $Q_n = \pm 1/3$, the number of configurations $Z_{1,N}$ differs from the number of ground states Z_N by some numerical factor w_1. We estimate the factor w_1 in the same naive way as we estimated the number of ground states; i.e., we assume that chiralities ± 1 have equal and independent probabilities. This yields $w_1 \approx 21/22$. The precision of this estimate is again of the order of 1/6, and we set in the following $w_1 = 1$. Denoting the long-wavelength part of $J(\mathbf{R})$ as $3K\Psi(\mathbf{R})$, where $K = \beta/12$, we arrive at the long-distance effective action in the standard form:

$$Z = \int D\Psi(\mathbf{r})$$

$$\times \exp\left\{-\int d^2\mathbf{r}\left[\frac{\sqrt{3}K}{2}(\nabla\Psi)^2 - ha^{-2}\cos(2\pi K\Psi)\right]\right\}, \quad (10)$$

where $h = 2e^{-K\pi^2/2} = 2e^{-\beta\pi^2/24}$ and $a = |\mathbf{a}|$. At the BKT transition temperature, this is a small field, which allows one to use the perturbative renormalization group approach [7]. The BKT transition occurs at the temperature where the field h becomes relevant. For the hexagonal lattice, we get $\sqrt{3}/2K_c = \pi/2$; i.e.,

$$T_c/\kappa S^2 = \sqrt{3}\pi/72 = 0.0756. \quad (11)$$

We neglected nonlinear terms which can slightly renormalize the stiffness constant. This effect on T_c is small because of the smallness of $T_c/\kappa S^2$ (see also [8]).

The existence of a new set of variables (chiralities) qualitatively changes the spin correlation function

compared to that in unfrustrated *XY* magnets. Returning to the initial formulation of the problem (2), we consider the correlation functions $\mathcal{H}_j(r_0) = \langle \exp(i[\theta(0) - \theta(\mathbf{r}_0)] \cdot j) \rangle$. In terms of the integer-valued variables, $n(\mathbf{r}, \mathbf{a})$, we arrive at an expression that differs from Eq. (4) only by arguments of the δ functions. Namely, for sites 0 and $\mathbf{r}_0$ we get

$$\sum_{\mathbf{a}} n(\mathbf{0}, \mathbf{a}) = -\sum_{\mathbf{a}} n(\mathbf{r}_0, \mathbf{a}) = j, \quad (12)$$

instead of the conservation condition (5). This condition is equivalent to the pattern of currents which is a superposition of currents $J(\mathbf{R}_h)$ flowing in the kagomé lattice and obeying the condition (5) and a current j, which takes a whole number value and which is created at the point $\mathbf{0}$ and annihilated at the point $\mathbf{r}_0$. Thus, the correlation function $\mathcal{H}_j(r_0)$ has the form

$$\mathcal{H}_j(r_0) = \frac{1}{Z(\beta)}$$

$$\times \sum_{\{J(\mathbf{R})\}} \prod_{(\mathbf{R} \neq \mathbf{R}^*, \mathbf{A} \neq \mathbf{A}^*)} I_{J(\mathbf{R}+\mathbf{A})+J(\mathbf{R})}(-\beta) \quad (13)$$

$$\times \prod_{(\mathbf{R}^*, \mathbf{A}^*)} I_{J(\mathbf{R}^*+\mathbf{A}^*)+J(\mathbf{R}^*)+j}(-\beta).$$

Here, $(\mathbf{R}^*, \mathbf{A}^*)$ are sites and vectors of the dual lattice such that $\mathbf{A}^*$ crosses the path $(\mathbf{0}, \mathbf{r}_0)$ on the initial kagomé lattice. Integrating over currents in the triangles in Eq. (13), we get $\mathcal{H}_j(r_0) = Z_j(\beta, r_0)/Z(\beta)$, where $Z(\beta)$ is given by Eq. (8) and $Z_j(\beta, r_0)$ differs from $Z(\beta)$ by the additional contribution from the current j running along the path $(\mathbf{0}, \mathbf{r}_0)$.

The contribution of $Q \neq 0$ configurations (vortex) to the large-r_0 asymptotic form of the spin correlation function $\mathcal{H}_j(r_0)$ below the BKT transition point is negligible, because the renormalization-group flow at $T < T_c$ makes the effective constant h in Eq. (10) equal to zero. The main difference between our $\mathcal{H}_j(r_0)$ and the usual (unfrustrated) case is in the factor

$$\exp\left(2\pi i \sum_{\mathbf{R}_t^*} \frac{\sigma(\mathbf{R}_t^*)}{3} \cdot j\right) \quad (14)$$

averaged over chiralities. For simplicity, we consider the case where the shortest walk on lattice sites between points 0 and r_0 goes over a straight line. In this case, r_0/a is the number of bonds along this walk, where a is the kagomé lattice constant. Neglecting constraints on chiralities of triangles, as we did before, we immediately get a factor of $(\cos 2\pi/3)^{r_0/a} = (-1)^{r_0/a} 2^{-r_0/a}$ in the correlation function if j is not a multiple of 3. Integration over $J(\mathbf{R}_h)$ in the $r_0 \longrightarrow \infty$ limit can be done in the spin-wave approximation, yielding the well-known

result [1]. Thus, in the low-temperature phase $T \leq T_c$ in the long-distance limit $r_0/a \gg 1$, and the spin correlation function reads

$$\mathcal{K}_j(r_0) \propto (-1)^{r_0/a} 2^{-r_0/a} (r_0/a)^{-j^2 T/36 T_c}, \quad (15)$$
$$j \neq 3, 6, 9, \ldots \, .$$

It decays exponentially with distance. Note that the statement about exponential decay of the spin–spin correlators does not depend on the approximations made here. This follows from the finiteness of the correlation length of the chirality field. The true order parameter of the BKT transition is the cubed spin [4] $\eta(\mathbf{r}) = \exp(3i\theta(\mathbf{r}))$. The correlation function of this order parameter at $T < T_c$ decays as a power of distance

$$\mathcal{K}_3(r_0) = \langle \eta(0)\eta^*(\mathbf{r}) \rangle \sim (r_0/a)^{-T/4T_c}. \quad (16)$$

The result for T_c is in agreement with Monte-Carlo simulations of the BKT transition in the kagomé antiferromagnet [6] and with recent independent calculations [11] (note that the preprint version of this paper was published before [12]). In [11], it is shown that the next-to-nearest-neighbor exchange interaction on the kagomé lattice can remove the ground-state degeneracy. However, the spin–spin interaction induced by thermal spin waves cannot play the same role. Indeed, in the case of the nearest-neighbor interaction considered here, spots of $\sigma(\mathbf{R})$ with changed signs have finite entropy at $T \longrightarrow 0$. Their contribution to the free energy and correlators dominates, and the effect of interaction induced by spin waves considered in [11] is negligible at low temperatures.

REFERENCES

1. V. L. Berezinskiĭ, Zh. Éksp. Teor. Fiz. **61**, 1144 (1971) [Sov. Phys. JETP **34**, 610 (1972)].

2. J. M. Kosterlitz and D. J. Thouless, J. Phys. C **6**, 1181 (1973).

3. V. V. Lebedev, Pis'ma Zh. Éksp. Teor. Fiz. **70**, 675 (1999) [JETP Lett. **70**, 691 (1999)]; Phys. Rev. E **62**, 1002 (2000).

4. D. A. Huse and A. D. Rutenberg, Phys. Rev. B **45**, 7536 (1992).

5. P. Chandra, P. Coleman, and I. Ritchey, J. Phys. I **3**, 591 (1993).

6. M. S. Rzchowskii, cond-mat/9508139.

7. J. V. Jose, L. P. Kadanoff, S. Kirkpatrick, and D. R. Nelson, Phys. Rev. B **16**, 1217 (1977).

8. A. Z. Patashinskiĭ and V. L. Pokrovskiĭ, *Fluctuation Theory of Phase Transitions* (Nauka, Moscow, 1983, 2nd ed.; Pergamon, Oxford, 1979).

9. A. A. Abrikosov, L. P. Gor'kov, and I. E. Dzyaloshinskii, *Methods of Quantum Field Theory in Statistical Physics* (Fizmatgiz, Moscow, 1962; Prentice-Hall, Englewood Cliffs, 1963).

10. R. J. Baxter, J. Math. Phys. **11**, 784 (1977).

11. S. E. Korshunov, cond-mat/0106463.

12. V. B. Cherepanov, I. V. Kolokolov, and E. V. Podivilov, cond-mat/9603115.

To the Memory of Our Contributors

PACS numbers: 01.60.+q

V.I. Belinicher *et al.*, Invariant Spin Coherent States and the Theory of a Quantum Antiferromagnet in a Paramagnetic Phase, JETP Lett. 72, 521 (2000).

Prof. Viktor Iosifovich Belinicher, an outstanding theoretical physicist, Doctor of Physics and Mathematics, a Leading Research Scientist at the Institute of Semiconductors SD RAS, Professor at Novosibirsk State University, perished at the age of 56 in the fatal Tel Aviv–Novosibirsk airplane accident that occurred on October 4, 2001.

V.I. Belinicher was a multiskilled theorist and made tangible contributions to various fields of physics. Elaboration of the theory of bulk photovoltaic effect has become his major achievement. V.I. Belinicher initiated experimental observation of the polarization-dependent effects in semiconducting crystals without an inversion center. This activity culminated in the discovery of a surface analogue of the bulk photovoltaic effect (surface photocurrent) and in the development of the theory of this effect. The resonant light drag effect is one of the more unusual phenomenon that was discovered and explained by V.I.B. and co-workers.

A sizable contribution was made by V.I.B. to the theory of hydrodynamic turbulence. In collaboration with V.S. L'vov, he formulated the scale-invariant form of this theory. The substitution of variables, found by them (currently known as the Belinicher–L'vov transformation), allowed the divergence to be eliminated in all orders of perturbation theory.

From the late 1980s and up to the last time, V.I. Belinicher was active in the problems of strongly correlated electronic systems, in particular, high-T_c superconductors. V.I.B. developed three major directions in this field: construction of a realistic electronic model for the copper oxide plane and use of this model for the calculation of the observed properties of high-T_c superconductors; spin-polaron aspect of high-T_s superconductivity and the nature of superconducting state; and the microscopic theory of two-dimensional antiferromagnetism. In particular, V.I.B., together with his collaborators, solved the problem of low-energy properties of the three-band Hubbard model, which is ordinarily used in the description of a system of copper oxide planes.

V.I. Belinicher was a brilliant theorist and mastered the most sophisticated methods of theoretical physics. He was highly self-exacting. V.I. did not accept double standards and evaluated his own works and the works of other authors only on the "Hamburg scale." He always endeavored to elevate the level of his work and, although was led to solve various problems in his life, he endeavored (especially in the last years) to concentrate on the most complex and fundamental physical problems. Viktor Iosifovich was highly active and had many projects. The tragedy over the Black Sea abruptly ended his activity which was in full swing.

L.I. Leonyuk *et al.*, New Scenario for the Decay of Spin-Peierls State in CuGeO$_3$: Fe. Onset of a Quantum Critical Point. JETP Lett. 73, 31 (2001).

Lidiya Ivanovna Leonyuk died on September 23, 2000 during her 50th year after serious illness. The scientific community lost an outstanding specialist in solid-state physics, crystallography, and crystal growth. Her last works were devoted to superconducting cuprates, compounds with ladder structure, and low-dimensional magnets and were a remarkable source of ideas, which have already make a great impact and continue to do so on current studies in these fields. L.I. Leonyuk, Doctor of Physics and Mathematics, the Director of the Laboratory of Crystal Growth at the Geological Department of Moscow State University, the author of more than 200 publications and two books, will be forever kept in the memory of her collaborators, who knew her as a remarkable enthusiastic scientist, an excellent experimenter, a women of unique cordiality, and a colleague, the scientific discourse with whom will now be sadly missed.

Translated by V. Sakun